The FEBS Journal

FEBS PRESS science publishing by scientists

Structural comparison of (hyper-)thermophilic nitrogenase reductases from three marine *Methanococcales*

Nevena Maslać[1], Cécile Cadoux[2,3], Pauline Bolte[1], Fenja Murken[1], Wenyu Gu[4], Ross D. Milton[2,3] and Tristan Wagner[1]

1 Microbial Metabolism Research Group, Max Planck Institute for Marine Microbiology, Bremen, Germany
2 Department of Inorganic and Analytical Chemistry, Faculty of Sciences, University of Geneva, Switzerland
3 National Centre of Competence in Research (NCCR) Catalysis, University of Geneva, Switzerland
4 Laboratory of Microbial Physiology and Resource Biorecovery, School of Architecture, Civil and Environmental Engineering, École Polytechnique Fédéral de Lausanne, Switzerland

Keywords
[4Fe–4S] cluster; nitrogen fixation; nitrogenase reductase; thermostability; X-ray crystallography

Correspondence
T. Wagner, Microbial Metabolism Research Group, Max Planck Institute for Marine Microbiology, Celsiusstraße 1, 28359 Bremen, Germany
Tel: +49 421 2028 7440
E-mail: twagner@mpi-bremen.de

(Received 16 August 2023, revised 17 January 2024, accepted 17 April 2024)

doi:10.1111/febs.17148

The nitrogenase reductase NifH catalyses ATP-dependent electron delivery to the Mo-nitrogenase, a reaction central to biological dinitrogen (N_2) fixation. While NifHs have been extensively studied in bacteria, structural information about their archaeal counterparts is limited. Archaeal NifHs are considered more ancient, particularly those from *Methanococcales*, a group of marine hydrogenotrophic methanogens, which includes diazotrophs growing at temperatures near 92 °C. Here, we structurally and biochemically analyse NifHs from three *Methanococcales*, offering the X-ray crystal structures from meso-, thermo-, and hyperthermophilic methanogens. While NifH from *Methanococcus maripaludis* (37 °C) was obtained through heterologous recombinant expression, the proteins from *Methanothermococcus thermolithotrophicus* (65 °C) and *Methanocaldococcus infernus* (85 °C) were natively purified from the diazotrophic archaea. The structures from *M. thermolithotrophicus* crystallised as isolated exhibit high flexibility. In contrast, the complexes of NifH with MgADP obtained from the three methanogens are superposable, more rigid, and present remarkable structural conservation with their homologues. They retain key structural features of P-loop NTPases and share similar electrostatic profiles with the counterpart from the bacterial model organism *Azotobacter vinelandii*. In comparison to the NifH from the phylogenetically distant *Methanosarcina acetivorans*, these reductases do not cross-react significantly with Mo-nitrogenase from *A. vinelandii*. However, they associate with bacterial nitrogenase when ADP·AlF_4^- is added to mimic a transient reactive state. Accordingly, detailed surface analyses suggest that subtle substitutions would affect optimal binding during the catalytic cycle between the NifH

Abbreviations
ADP, adenosine diphosphate; AMPPCP, adenosine-5′-[(β, γ)-methyleno]triphosphate; ATP, adenosine triphosphate; AU, Asymmetric unit; *Av*AnfH, *Azotobacter vinelandii* AnfH; *Av*NifDK, *Azotobacter vinelandii* NifDK; *Av*NifH, *Azotobacter vinelandii* NifH; *Av*VnfH, *Azotobacter vinelandii* VnfH; *Cp*NifH, *Clostridium pasteurianum* NifH; CV, column volume; DEAE, diethylaminoethyl; DNase, deoxyribonuclease; DT, dithionite; DTT, dithiothreitol; EDTA, ethylenediaminetetraacetic acid; FeMoco, FeMo-cofactor; HIC, hydrophobic interaction chromatography; hrCN PAGE, high resolution clear native polyacrylamide gel electrophoresis; IEX, ion exchange chromatography; IPTG, isopropyl β-D-1-thiogalactopyranoside; *Ma*NifH, *Methanosarcina acetivorans* NifH; *Ma*VnfH, *Methanosarcina acetivorans* VnfH; *Mi*NifH, *Methanocaldococcus infernus* NifH; *Mm*NifH, *Methanococcus maripaludis* NifH; MOPS, 3-(*N*-morpholino)propanesulfonic acid; *Mt*NifH, *Methanothermococcus thermolithotrophicus* NifH; Ni-NTA, nickel-nitrilotriacetic acid; NTPase, nucleoside-triphosphatase; PBS, phosphate-buffered saline; PDB, Protein Data Bank; Rmsd, root mean square deviation; SDS/PAGE, sodium dodecyl sulfate polyacrylamide gel electrophoresis; TB salts, terrific broth salts; TRIS, tris(hydroxymethyl)aminomethane.

from *Methanococcales* and the bacterial nitrogenase, implying differences in the N_2-machinery from these ancient archaea.

Introduction

Nitrogen, a key element for Life, is ubiquitous in the atmosphere in the form of dinitrogen (N_2), although it is not readily bioavailable and must be converted to its most reduced state: ammonium (NH_4^+) for efficient biological assimilation [1]. N_2 is mostly reduced through the industrial Haber–Bosch process and by biological N_2-fixation via nitrogenases, the only known class of enzymes able to catalyse this reaction. The Haber–Bosch process plays a major role in supporting global agriculture, with 80–85% of the produced NH_3 used as fertiliser [2,3] for crops feeding half the world's population [4]. While this artificial process is essential to sustain our modern society, it has significant drawbacks, such as high energy consumption and fossil fuel dependency to obtain H_2, resulting in the release of the greenhouse gas CO_2 [5,6]. The high-energy requirements and harsh conditions of this process are due to the high kinetic stability of the N_2 triple bond (with a bond energy of 941 $kJ{\cdot}mol^{-1}$) [7]. In the search for sustainable, robust, and effective alternative catalysts [2,8], researchers study biological N_2-fixation for application and bioinspiration. Nitrogenases are remarkable enzymes performing N_2-fixation under ambient conditions, and considerable efforts over the past decades have been made to obtain insights into their catalytic cycle, serving as blueprints to design new catalysts through biomimicry, which first requires a detailed understanding of nitrogenase's catalytic mechanism [9].

Nitrogenases are metalloenzymes made of two components: NifDK (also referred to as the MoFe protein or the dinitrogenase) and NifH (referred to as the Fe protein or the nitrogenase reductase). The heterotetrameric NifDK ($\alpha_2\beta_2$) contains two metalloclusters: an [8Fe-7S] P-cluster and a [7Fe-9S-C-Mo]:homocitrate FeMo-cofactor (FeMoco), the latter being the catalyst and representing the most complex metallocofactor currently known in biology [10–12]. Two other nitrogenase isoforms exist in which the molybdenum is exchanged for a vanadium or an iron atom instead [7,13]. These two other isoforms, considered to have evolved from NifDK, are encoded in different operons, harbouring a different set of Fe proteins (VnfH and AnfH for the V and Fe system, respectively), chaperones involved in cofactor biosynthesis, and partners with still elusive functions [14–16].

All known Fe proteins belong to the P-loop NTPase superfamily and form homodimers, with each monomer folded as a single α/β-type domain containing a nucleotide-binding site [17,18]. A typical cubane [4Fe–4S] cluster bridges the homodimer and is coordinated by 2 x Cys residues from each subunit [12,19]. NifH acts as an electron donor to NifDK for N_2 fixation and is required in FeMoco biosynthesis and apo-NifDK maturation [20,21]. The binding of a reduced NifH loaded with MgATP to the NifDK is thought to lower the reduction potential of the P cluster, triggering unidirectional electron transfer to the FeMoco in a so-called 'deficit-spending mechanism' [21–24]. The vacant electron is then replenished by electron transfer from the [4Fe–4S] cluster of NifDK-bound NifH and requires the hydrolysis of two ATP molecules [22]. The subsequent phosphate release has been shown to be the rate-limiting step in the nitrogen reduction cycle [25]. NifH then dissociates from NifDK, proceeds to the nucleotide exchange and is reduced back by either ferredoxin [26] or a flavodoxin [27]. This elegant ballet of electron transfer and nucleotide exchange is schematised in Fig. 1. Following the Lowe-Thorneley model [28], a minimum of 8 cycles is required to accomplish the complete reduction of one N_2 molecule by NifDK, which leads to the hydrolysis of 16 ATP (Fig. 1) [13,29,30].

Electron transfer to the substrate and ATP hydrolysis have constant rates, irrespective of the molecule undergoing reduction [31]. Indeed, in addition to dinitrogen, nitrogenase can reduce a variety of other substrates, including acetylene, hydrogen cyanide, thiocyanate, azide ions, methyl isocyanide and carbon monoxide [32]. The respective affinity for these substrates fluctuates depending on the isoform [33,34]. NifH can also act as a reductase on its own, catalysing the reduction of CO_2 to CO [35] and even further reducing CO to hydrocarbons, albeit at low rates [36]. This feature is particularly important for the development of CO_2 remediation strategies.

Despite being of great interest for biotechnology, the structural information gathered for the Fe-protein is limited to the bacteria *Azotobacter vinelandii* [19,37,38] and *Clostridium pasteurianum* [39] and the archaeon *Methanosarcina acetivorans* [40].

In contrast, the NifH homologues from *Methanococcales*, considered more ancient and phylogenetically

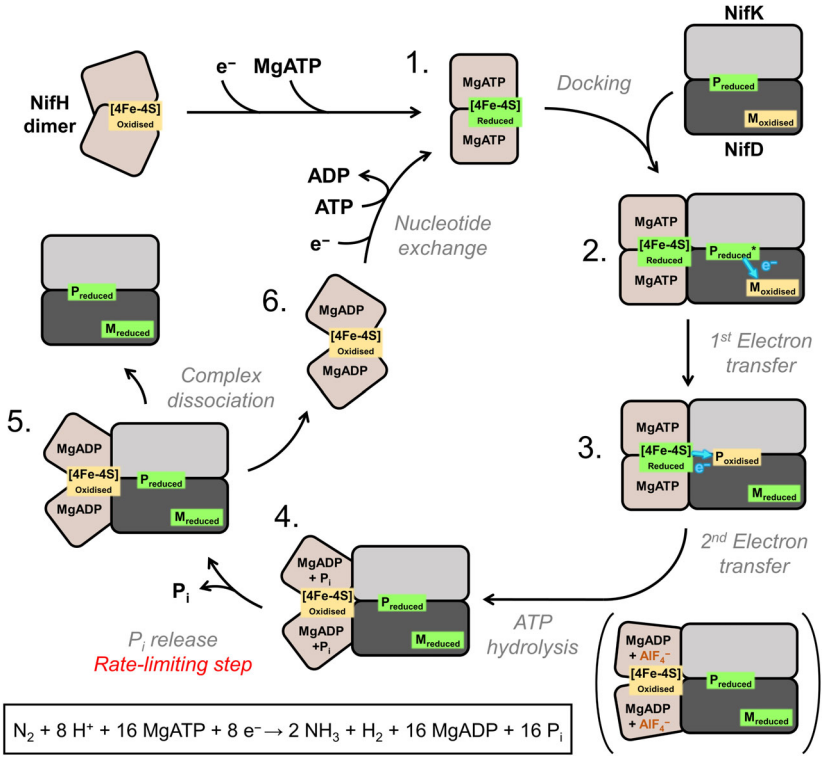

Fig. 1. Order of events for the nitrogenase catalytic cycle during a single turnover and according to the 'deficit spending model' [23,94] and based on [95]. The scheme depicts the six different states (labelled as 1–6) of the NifH cycle. NifH is shown as a homodimer loaded with a reduced [4Fe–4S] cluster and MgATP in its active state (state 1). Only one-half of the NifDK heterotetramer is displayed for clarity, with whom NifH associates (state 2). The redox states are simplified as single electron 'reduced'/'oxidised' states based on [59]. NifDK-NifH association triggers an electron transfer (state 2 to 3) from the activated P-cluster (labelled as P*) to the FeMoco (labelled as M). A second electron transfer follows from the reduced [4Fe–4S] cluster of NifH to the oxidised P cluster, and the ATP is hydrolysed (state 3 to 4). This leads to the NifH homodimer containing 2MgADP/2P_i and the oxidised [4Fe–4S] cluster (state 4). The artificial complex of NifDK-NifH with NifH in complex with MgADP and AlF_4^- mimics this intermediate transition in which the [4Fe–4S] cluster is adequately positioned for electron transfer to the P-cluster [58,59]. After P_i release (state 4 to 5), NifH-MgADP disengages from NifDK (state 6) and can be reloaded with an electron and ATP to start a new cycle.

distant from *Methanosarcina* [41,42], present new interesting perspectives for the field. *Methanococcales* are hydrogenotrophic methanogens (feeding on H_2 and CO_2) exclusively marine, with species showing a growth optimum ranging from 20 °C to 98 °C [43–46]. Metagenomic and metatranscriptomic studies have concluded that *Methanococcales* are actively contributing to the N_2-fixation process in some ecological niches [47–50]. They exhibit impressive diazotrophic abilities under laboratory conditions [42,51]. For instance, *Methanocaldococcus vulcanius* holds the world record for the highest temperature for N_2-fixation and *Methanothermococcus thermolithotrophicus* presents resistance to tungstate under diazotrophic conditions [42,52]. These strictly anaerobic (hyper)-thermophiles must rely on thermostable nitrogenases, which represent candidates for novel bioinspired catalysts capable of withstanding harsh industrial conditions [53].

Here, we report the first structural insights into NifH from methanogens belonging to the *Methanococcales* order: the mesophilic *Methanococcus maripaludis* (*Mm*NifH) [54], the thermophilic *M. thermolithotrophicus* (*Mt*NifH) [55] and the hyperthermophilic *Methanocaldococcus infernus* (*Mi*NifH) [56]. Combining biochemical and structural analyses, we unveil their specific properties and examine their cross-reactivity with the distant bacterial model from *A. vinelandii*.

Results

Position of NifHs from *Methanococcales* and structural homologues in the phylogenetic tree

The neighbour joined protein tree of selected NifH, VnfH and AnfH sequences branches in two main NifH lineages: the base-branching NifH containing some

hydrogenotrophic methanogens (including the protein from *M. maripaludis*) and the more diversified and recent [41] group containing sequences found in bacteria and archaea, with most of Anf and Vnf gathering in a single monophyletic branch (Fig. 2A and Table S1). This clustering is consistent both with the previously described concatenated NifDKH protein trees [15,41] and individually observed subunits [42]. It is also one of the main arguments in favour of the currently accepted theory that the Nif system evolved in hydrogenotrophic methanogens [14] and that Nif predates the Vnf and Anf systems [15,41]. Hence, these Nif systems found in methanogens such as *M. maripaludis* are particularly intriguing as they are closer to the roots of the phylogenetic tree, suggesting a more ancient origin and, maybe, ancestral features. In accordance with the phylogenetic tree, *Mt*NifH and *Mi*NifH are highly similar and share 85.16% of sequence identity, while *Mm*NifH shares roughly 73% identity with them (Fig. 2B). The three sequences are closer to *Av*AnfH (in the range of 74% sequence identity) compared to *Av*NifH or *Av*VnfH.

*Mm*NifH, *Mt*NifH and *Mi*NifH were further biochemically investigated due to their distinct and unique phylogenetic positions, but also to study the basis of their thermo-adaptation.

NifHs from *Methanococcales* share the typical P-loop NTPase fold

Following our improved protocol, diazotrophic *M. thermolithotrophicus* and *M. infernus* were cultivated at a large scale (see Materials and methods). *Mt*NifH and *Mi*NifH were successfully natively purified under anaerobic conditions through three chromatographic steps, yielding satisfying enrichment for structural attempts (Fig. S1A). The NifH homologue from *M. maripaludis* was recombinantly expressed using *Escherichia coli* as a host (see Materials and methods). Since the required quantities for activity assays were not compatible with the yield obtained from native purification, *Mt*NifH/*Mi*NifH were additionally recombinantly produced in *E. coli* (Fig. S1B).

The structure of nucleotide-free *Mt*NifH was obtained in two crystal forms, a monoclinic $P2_1$ (form 1) and a tetragonal $P4_32_12$ (form 2), refined to 2.31 and 1.91 Å, respectively (Table 1 and Fig. S2). *Mm*NifH and *Mi*NifH were tentatively crystallised as isolated but did not yield exploitable crystals. However, crystals were obtained for the three proteins in the presence of MgADP. The MgADP-bound structures (Fig. 1, state 6) of *Mm*NifH, *Mt*NifH and *Mi*NifH were refined to 1.70, 2.74 and 2.49 Å, respectively (Table 1).

All structural features previously described as essential for NifH functionality are conserved in all three methanogenic systems. Figure 3A displays a sequence alignment from ESPript (https://espript.ibcp.fr, [57]) using the model of *Mt*NifH as input, highlighting the 11 α-helices and 8 β-sheets, which organise in the Rossmann fold characteristic for the P-loop NTPases (Fig. 3B). The P-loop, switch I and switch II, hallmarks of P-loop NTPases, are perfectly conserved (Fig. 3A) reflecting the critical importance of these motifs for functionality. The P-loop (residues 17–24 in *Mt*/*Mi*NifH and 9–16 in *Mm*NifH) plays a major role in the coordination of the bound nucleotides and Mg^{2+} and goes through conformational changes upon ligand binding together with switch I (residues 46–52 in *Mt*/*Mi*NifH and 38–44 in *Mm*NifH, also participating in Mg^{2+} coordination) and switch II (residues 133–140 in *Mt*/*Mi*NifH and 125–132 in *Mm*NifH) regions. Switch II is directly involved in [4Fe–4S] cluster coordination and stabilises the P-loop through two anchoring points: S16-D125/G11-D129 in *Mm*NifH and S24-D133/G19-D137 in *Mt*/*Mi*NifH (Figs 4 and 5).

The structures of *Mt*NifH in the nucleotide-free state are flexible, especially at the dimeric interface (Fig. 4A,C,D), compared to the locked conformation when complexed with nucleotides. The nucleotide binding restraining the natural flexibility of Fe-proteins has already been mentioned in previous works [58,59] and is illustrated in Fig. 4D.

In an attempt to identify structural features contributing to the thermostability of *Mt*NifH and *Mi*NifH homodimers, we used the PISA server [60] to quantify the free energy of assembly dissociation (ΔG^{diss}), which is expected to increase proportionally to the temperature. The analyses, performed on all MgADP-bound states, surprisingly showed that the hyperthermophilic *Mi*NifH has the smallest average ΔG^{diss} (21.5 kcal·mol^{-1}) (Table 2), while *Av*NifH has the largest (37.4 kcal·mol^{-1}). In this regard, *Av*NifH also has the greatest number of salt bridges (14), while *Mt*NifH and *Mi*NifH have fewer salt bridges than *Mm*NifH. Accordingly, the number of intrachain salt bridges also decreases when comparing the NifH originating from mesophile, thermophile and hyperthermophile (Table 2).

The thermostability of the four NifHs was tested *in vitro*. An anaerobic assay was set up, and the melting point (T_m) determined for *Av*NifDK of 59.2–60.1 °C (Fig. 6A and Fig. S3) was similar to that determined by circular dichroism in our recent work (≈57 °C) [61]. As expected from the *in silico* analyses, *Av*NifH has a greater T_m (67.6 °C) than *Mm*NifH and *Mt*NifH (51.5

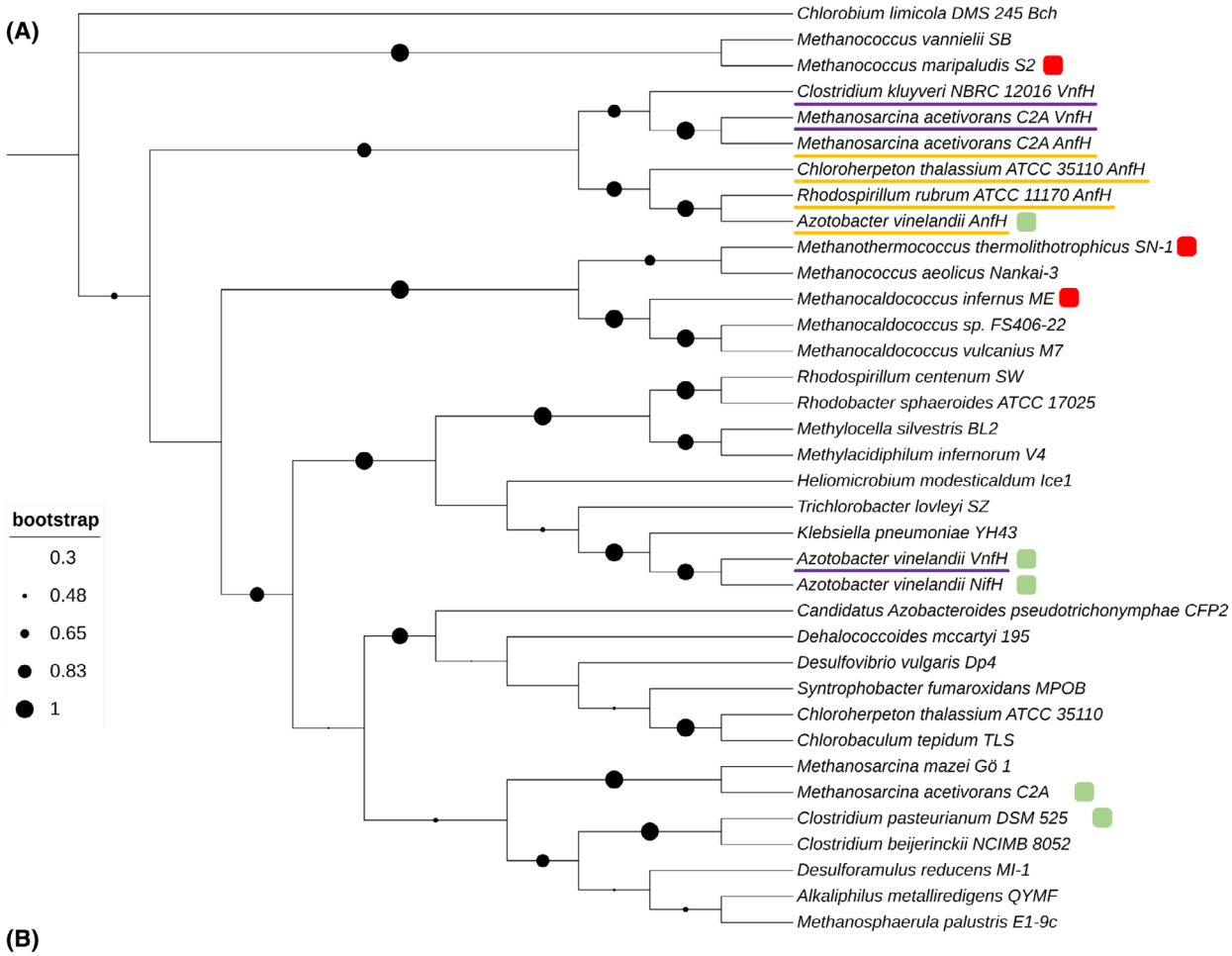

(B)

% identity	*Av*NifH	*Av*VnfH	*Av*AnfH	*Cp*NifH	*Ma*NifH	*Mm*NifH	*Mt*NifH	*Mi*NifH
*Av*NifH	100.00	91.35	64.23	69.09	64.73	65.09	63.64	63.87
*Av*VnfH		100.00	64.96	66.91	65.09	64.36	63.27	63.87
*Av*AnfH			100.00	64.10	66.30	75.27	75.09	73.72
*Cp*NifH				100.00	71.17	63.87	63.87	61.54
*Ma*NifH					100.00	62.04	62.41	62.64
*Mm*NifH						100.00	73.26	72.89
*Mt*NifH							100.00	85.16
*Mi*NifH								100.00

Fig. 2. Phylogenetic analysis and sequence conservation of NifH from *Methanococcales* and homologues. (A) Evolutionary analysis of 35 selected NifH/VnfH/AnfH sequences. Node statistics are represented by black dots whose diameter depends on the node score (see bootstrap legend). Structures currently available and presented in this work are highlighted with green and red rounded squares, respectively. VnfHs and AnfHs are underlined in purple and orange, respectively. ChlL (light-independent protochlorophyllide reductase) from *Chlorobium limicola* was used as an outgroup. Accession numbers for sequences used in phylogenetic reconstruction can be found in Table S1. The tree was constructed in MEGA11 and visualised and annotated with ITOL v5 [93]. (B) Sequence identity matrix between structurally characterised Fe proteins. Colour code: red-green from the lowest to the highest percentage identity value.

Table 1. Data collection and refinement statistics.

	*Mt*NifH as isolated form 1	*Mt*NifH as isolated form 2	*Mm*NifH-MgADP	*Mt*NifH-MgADP	*Mi*NifH-MgADP
Data collection					
Synchrotron source	SOLEIL, Proxima-I	SOLEIL, Proxima-I	SLS, PXIII	SLS, PXIII	SLS, PXI
Wavelength (Å)	1.74013	1.74013	0.99999	1.00004	0.99999
Space group	$P2_1$	$P4_32_12$	$P2_1$	$P1$	$P2_12_12_1$
Resolution (Å)	68.14–2.31 (2.35–2.31)	52.00–1.91 (1.94–1.91)	78.82–1.70 (1.86–1.70)	71.00–2.74 (2.90–2.74)	120.26–2.49 (2.83–2.49)
Cell dimensions					
a, *b*, *c* (Å)	52.82, 83.98, 116.60	98.90, 98.90, 61.13	68.55, 111.09, 78.82	61.48, 87.59, 182.05	147.95, 156.73, 206.45
α, β, γ (°)	90, 91.14, 90	90, 90, 90	90, 90.01, 90	93.98, 98.58, 109.65	90, 90, 90
R_{merge} (%)[a]	24.0 (134.2)	15.9 (312.0)	21.9 (123.2)	28.4 (122.4)	17.6 (231.4)
R_{pim} (%)[a]	8.5 (56.6)	2.5 (64.4)	9.0 (51.1)	11.7 (50.9)	4.0 (52.9)
$CC_{1/2}$[a]	0.990 (0.517)	0.997 (0.616)	0.992 (0.468)	0.983 (0.526)	0.998 (0.680)
I/σ_I[a]	5.2 (1.5)	15.9 (1.4)	7.5 (1.6)	4.5 (1.6)	15.5 (2.0)
Spherical completeness[a]	100 (100)	100 (100)	73.5 (15.9)	72.1 (22.8)	54.4 (8.6)
Ellipsoidal completeness[a]	/	/	94.2 (57.6)	90.5 (63.1)	91.2 (77.5)
Redundancy[a]	8.7 (6.5)	41.2 (23.9)	6.9 (6.6)	6.7 (6.7)	20.8 (19.3)
Nr. unique reflections[a]	45 087 (2223)	24 200 (1183)	94 344 (4718)	66 142 (3154)	91 224 (4487)
Refinement					
Resolution (Å)	48.47–2.31	52.01–1.91	46.89–1.70	39.93–2.74	49.26–2.49
Number of reflections	45 074	24 197	94 335	66 105	91 144
R_{work}/R_{free}[b] (%)	19.63/23.49	20.32/23.05	16.18/18.59	21.90/25.43	22.20/24.20
Number of molecules/AU	4	1	4	12	12
Number of atoms	8969	2278	10 139	25 980	26 165
Protein	8545	2123	8598	25 495	25 660
Ligands/ions	46	29	205	462	464
Solvent	378	126	1336	23	41
Mean *B*-value ($Å^2$)	37.92	46.31	20.79	60.62	79.27
Molprobity clash score, all atoms	4.08	1.86	1.66	2.56	2.61
Ramachandran plot					
Favoured regions (%)	97.92	97.09	98.38	97.45	98.41
Outlier regions (%)	0	0	0	0.06	0.03
rmsd[c] bond lengths (Å)	0.006	0.013	0.009	0.009	0.009
rmsd[c] bond angles (°)	0.874	1.431	0.913	1.239	1.258
PDB ID code	8Q5T	8Q50	8Q5X	8Q5V	8Q5W

[a]Values relative to the highest resolution shell are within parentheses.; [b]R_{free} was calculated as the R_{work} for 5% of the reflections that were not included in the refinement.; [c]rmsd, root mean square deviation.

and 52.4 °C, respectively). However, *Mi*NifH presents an impressively high T_m of 82.5 °C, attesting to its thermostability. Since *Mt*NifH and *Mi*NifH have the same length and have been produced and tagged in the same way, we inspected the amino-acid substitutions to rationalise the T_m shift of 30 °C (Fig. 6B).

In *Mi*NifH, the most prominent substitutions are exposed to the surface and include five residues that were substituted by glycines (four at the start/end of the loop, and one in a helix) and one substitution which led to the apparition of a proline at the start of a helix. In addition, some hydrophilic residues pointing

Fig. 3. Secondary structure conservation of NifHs from *Methanococcales* and homologues. (A) Sequence alignment of *Mt*NifH, *Mi*NifH, *Mm*NifH, *Ma*NifH (PDB 6NZJ), *Av*AnfH (PDB 7QQA), *Av*NifH (PDB 2NIP), *Av*VnfH (PDB 6Q93), and *Cp*NifH (PDB 1CP2). The alignment was done by MUSCLE [88], while the conserved residues and the corresponding secondary structures (following the nomenclature of [39]) were analysed by ESPRIPT [57] on the structure of *Mt*NifH. (B) Secondary structures of *Mt*NifH monomer (as isolated, form 2) labelled based on ESPRIPT. The chain is coloured as a rainbow ranging from the N- (blue) to the C-terminus (red).

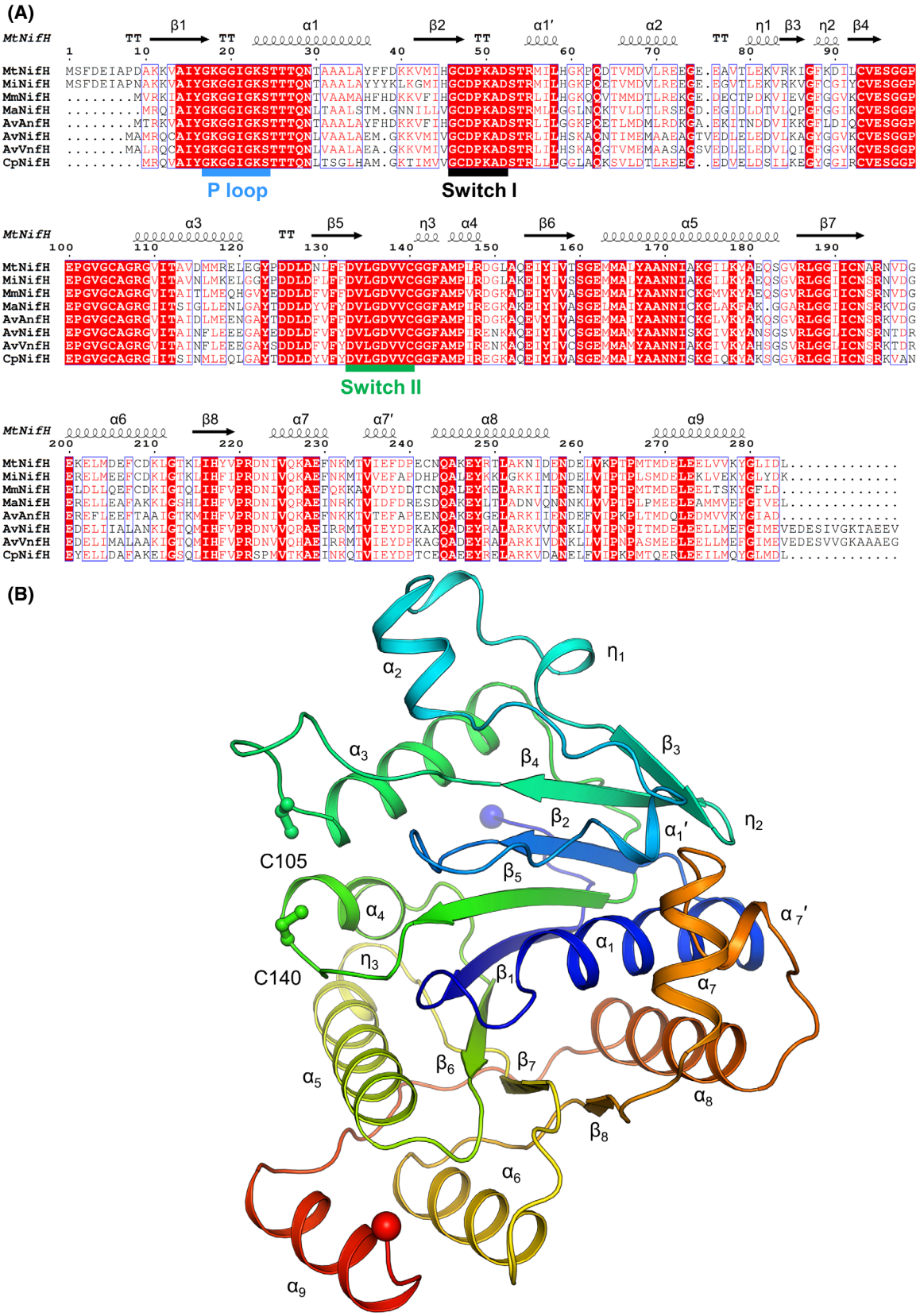

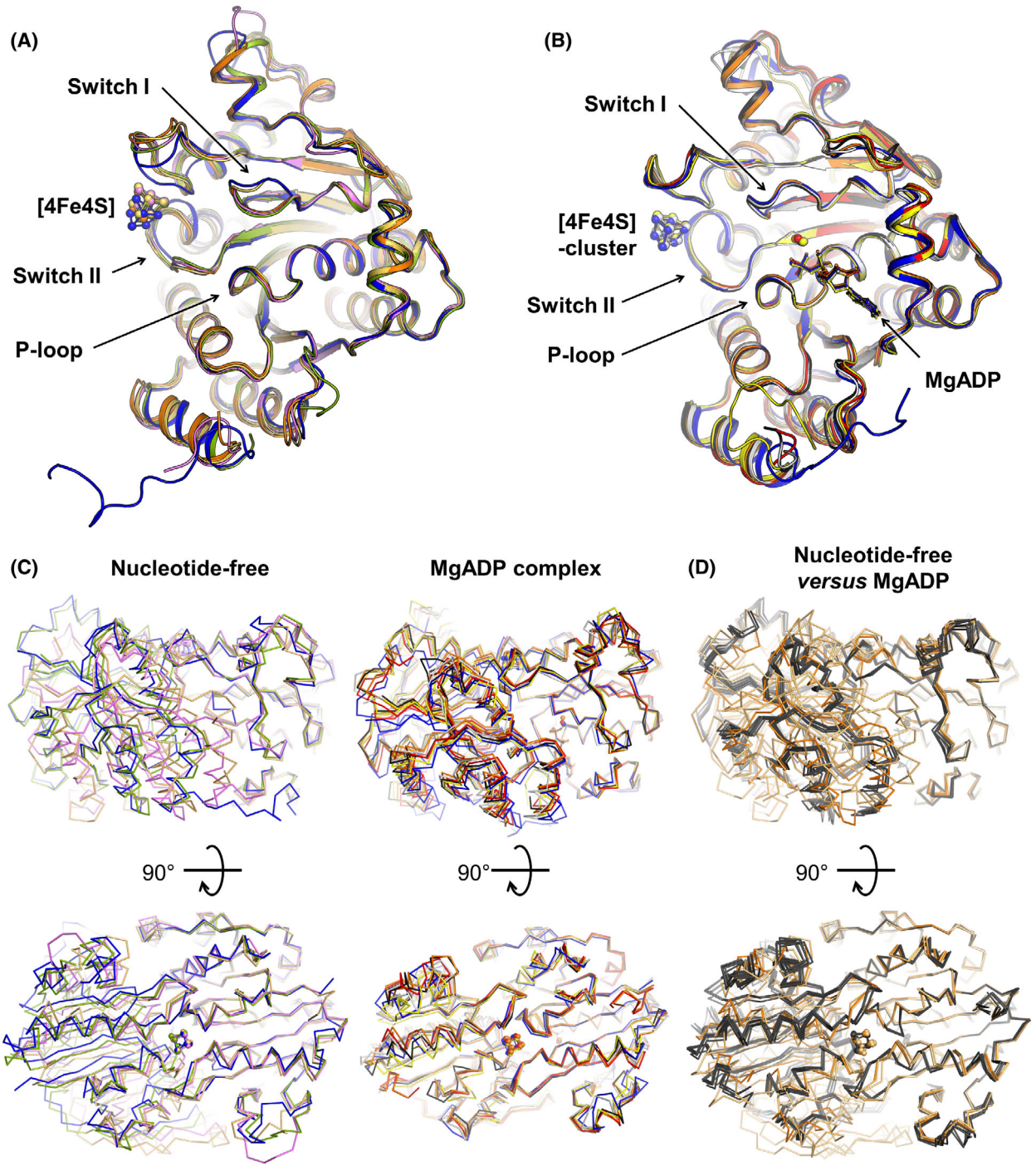

Fig. 4. Impact of nucleotide binding on nucleotide and [4Fe–4S] cluster coordinating motifs of NifH from *Methanococcales* and homologues and their flexibility. (A) Superposition of nucleotide-free monomer from *Mt*NifH form 1 (dark yellow) and form 2 (orange), *Ma*NifH (PDB: 6NZJ, violet), *Cp*NifH (PDB: 1CP2, split-pea) and *Av*NifH (PDB: 2NIP, blue). (B) Superposition of MgADP bound monomer from *Mm*NifH (yellow), *Mt*NifH (orange), *Mi*NifH (red), *Av*NifH (PDB: 6N4L, blue), *Av*VnfH (PDB: 6Q93, white) and *Av*AnfH (PDB: 7QQA, black), in the same pose as panel (A). All models are pictured in cartoons with ligands in balls and sticks. (C) Left: side and top views of NifH homodimers nucleotide-free with the same models and colour coding as in panel (A). Right: side and top views of MgADP-bound NifH homodimers with the same models and colour-coding as in panel (B). (D) Superposition of nucleotide-free *Mt*NifH form 2 (orange), with the two homodimers occupying the asymmetric unit of form 1 (dark yellow) and the six MgADP-bound *Mt*NifH homodimers occupying the asymmetric unit (black). For (C and D), all models displayed as ribbons were superposed on the right *Mt*NifH monomer (form 2 for the nucleotide-free).

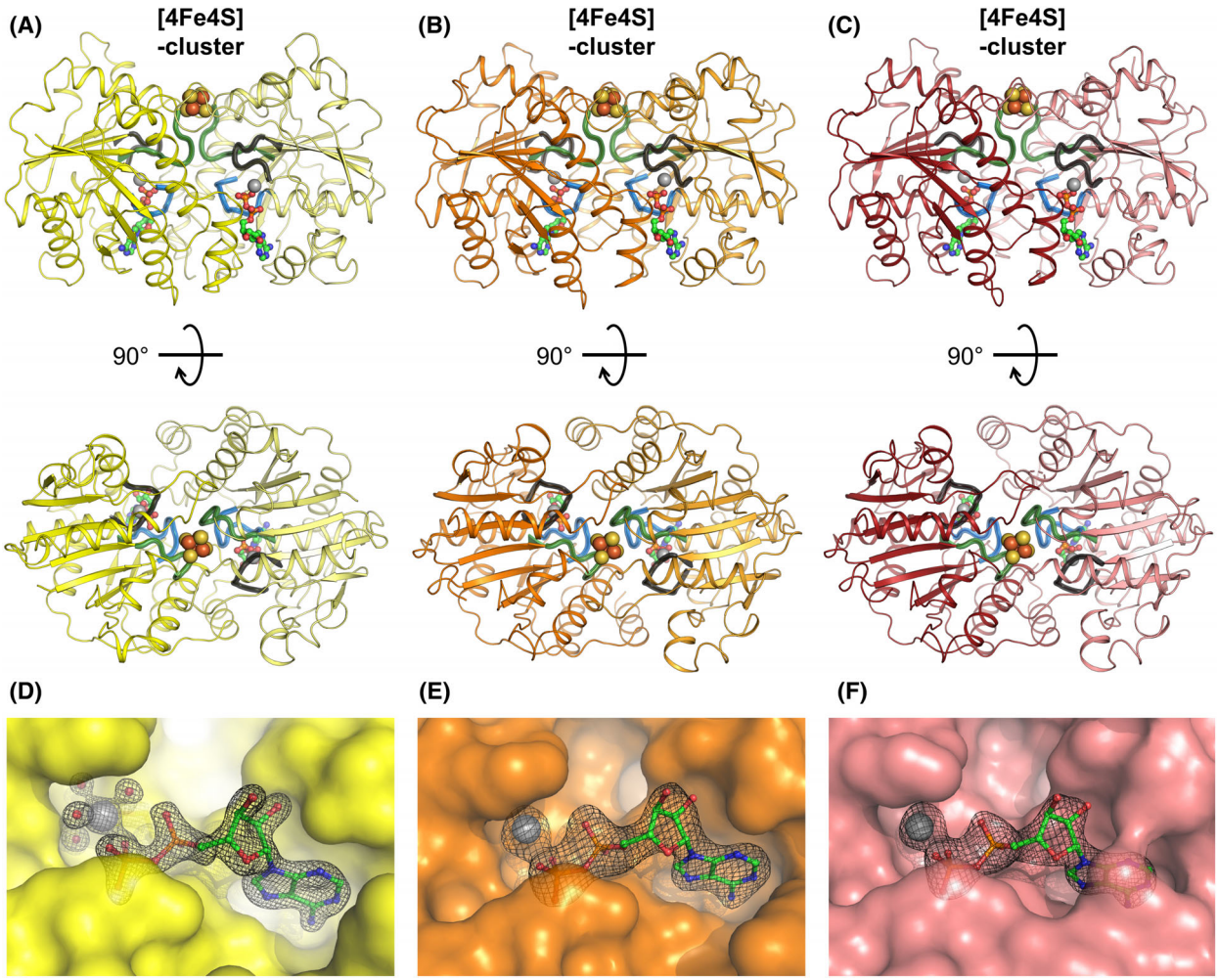

Fig. 5. Structures and ligand binding sites of MgADP-bound *Mm*NifH, *Mt*NifH and *Mi*NifH homodimers. (A–C) Side and top views of MgADP-bound *Mm*NifH (A, yellow), *Mt*NifH (B, orange) and *Mi*NifH (C, red). Homodimers are displayed in cartoons with one monomer in a fainter colour than the other. Important structural features are colour-coded as follows: Switch I – black, Switch II – green, and P-loop –blue. (D–F) Electron density of MgADP within the ligand binding site in *Mm*NifH (D, yellow), *Mt*NifH (E, orange) and *Mi*NifH (F, light red). A surface represents the proteins. All electron density maps ($2F_o-F_c$) are contoured to 2-σ. Due to the lower resolution of the models, waters were not modelled in (E and F) panels. All ligands are depicted in ball and stick models with carbon, nitrogen, oxygen, phosphorus, magnesium, sulphur and iron coloured in green, blue, red, orange, grey, yellow and dark orange.

to the core of the protein in *Mt*NifH were substituted by hydrophobic residues in *Mi*NifH (e.g., the hydrophobic cluster Leu40, Phe129, and Met256 in *Mi*NifH). We hypothesise that the combination of features might fortify the hydrophobic core while allowing more flexibility at strategic structural positions.

The [4Fe–4S] cluster and ligand-binding sites are conserved in NifHs from *Methanococcales*

[4Fe–4S] cluster occupancies and redox states were measured by spectrophotometry (Fig. 7). The four tested NifHs exhibit the typical profile of an [4Fe–4S] cluster containing proteins [62]. Based on this measurement, the [4Fe–4S] occupancy has been estimated to be 85%, 71%, and 73% for *Mm*NifH, *Mt*NifH, and *Mi*NifH, respectively. The proteins were all in an oxidised state, based on their subsequent reduction by dithionite addition (e.g., dithionite led to a decrease of absorption in the range of 400–550 nm, Fig. 7).

The [4Fe–4S] cluster at the interface of the NifH homodimers is coordinated by Cys97/Cys132 in *Mm*NifH and Cys105/Cys140 *Mt*NifH/*Mi*NifH (Fig. 3). The close environment of the [4Fe–4S] cluster is perfectly conserved, including the arginine (Arg100

Table 2. Analysis of the interface stability in different NifH homologues. N_{HB}, number of hydrogen bonds; N_{SB}, number of salt bridges; T °C, optimal temperature for the host growth; ΔG^{diss}, the free energy of assembly dissociation.

	*Av*NifH (6N4L)	*Av*VnfH (6Q93)	*Av*AnfH (7QQA)	*Mm*NifH	*Mt*NifH	*Mi*NifH
T °C	30 °C	30 °C	30 °C	37 °C	65 °C	85 °C
At the dimeric interface only						
ΔG^{diss} [kcal/mol]	37.4	25.8 ± 4.0	23.8 ± 0.4	24.2 ± 2.2	24.2 ± 1.3	21.5 ± 1.1
N_{HB}	14	12 ± 1	7 ± 4	18 ± 1	9 ± 1	9 ± 2
N_{SB}	14	7 ± 3	3 ± 1	10 ± 2	6 ± 2	8 ± 1
Intrachain salt bridges						
N_{SB} intrachain considering only Arg, Lys, Glu, Asp	15.0	9.6 ± 1.9	13.0 ± 2.2	15.2 ± 1.7	11.9 ± 2.0	10.6 ± 3.0

in *A. vinelandii*), which is participating in CO_2 reduction [40].

Based on the electron density map, the MgADP fully occupies the ligand-binding pocket in the three structures (Fig. 5). Due to their perfect sequence conservation, it was expected that the P-loop, switch I and II, and the residues involved in ligand binding would exhibit similar three-dimensional conservation. Our three models corroborate this hypothesis, and Fig. 8 details the identical ligand binding network across the bacterial and archaeal NifHs. A slight deviation was observed in the recombinantly produced *Mm*NifH, in which a C-terminal extension was introduced to add a His-tag. Here, the Arg213, which should stack the adenine ring together with Val217, has been displaced by the artificially Arg277, stabilised by the Asp275 and Ser186. Despite this exchange, the overall geometry of the ADP is unaffected (Fig. 8B).

The comparative analysis of the electrostatic surfaces between the NifHs from *Methanococcales* and the three Fe proteins from *A. vinelandii* presents an overall similar charge distribution pattern with a positive patch around the [4Fe–4S] cluster and a negatively charged outer ring (Fig. 9, top view). This general pattern is common among all studied Fe proteins, including Vnf and Anf systems. While *Mm*NifH and *Mi*NifH have two distinct positive patches on the outer ring, we presume that the electrostatic surface charges should still be complementary enough to that of *Av*NifH and would therefore support cross-reactivity with *Av*NifDK as previously shown for *Av*VnfH and *Av*AnfH [37,38].

NifHs from *Methanococcales* are not active *in vitro* when combined with *Av*NifDK

Cross-reactivity experiments have been conducted previously, e.g., N_2-fixation activity between a Fe protein and a MoFe protein from a different system or organism [38,63,64]. These studies confirmed that *Av*VnfH and *Av*AnfH and the two isoforms from *Methanosarcina acetivorans* (*Ma*NifH and *Ma*VnfH) can cross-react with *Av*NifDK albeit exhibiting lower rates. To monitor the cross-reactivity between the NifHs from the *Methanococcales* and the bacterial NifDK, we tested the physiological reaction of N_2-reduction by quantifying the final reaction product, NH_4^+. The NifH proteins used in the assay were produced recombinantly to circumvent the yield limitations of native purification. NifDK and NifH from *A. vinelandii* were purified as previously described [65] and served as a positive control for the reaction.

Despite our attempts, we could not detect any reliable activity for the enzymes from *Methanococcales* even when these proteins were used immediately after their purification without any freezing steps (Fig. 10). Since the affinity of these NifHs for *Av*NifDK might be relatively low, we increased the molar ratio of NifDK : NifH up to 1 : 50. Here again, no activities could be detected when compared to the negative controls. *Mt*NifH : *Av*NifDK at a molar ratio of 1 : 50 resulted in 8.2% of the activity measured with *Av*NifH. However, this relative activity must be considered cautiously since the negative controls also exhibit a slight background (Fig. 10).

The apparent incompatibility between the methanogenic NifHs and *Av*NifDK prompted the question of whether, despite the seemingly overall conserved interaction interface, there are indeed subtle differences in singular residues causing it and whether the complex between the two can be formed.

MgADP·AlF_4^- addition allows nitrogenase docking

To check if *Mm*/*Mt*/*Mi*NifHs can form a complex with *Av*NifDK, we incubated the different proteins coupled with MgADP·AlF_4^- and observed the complex

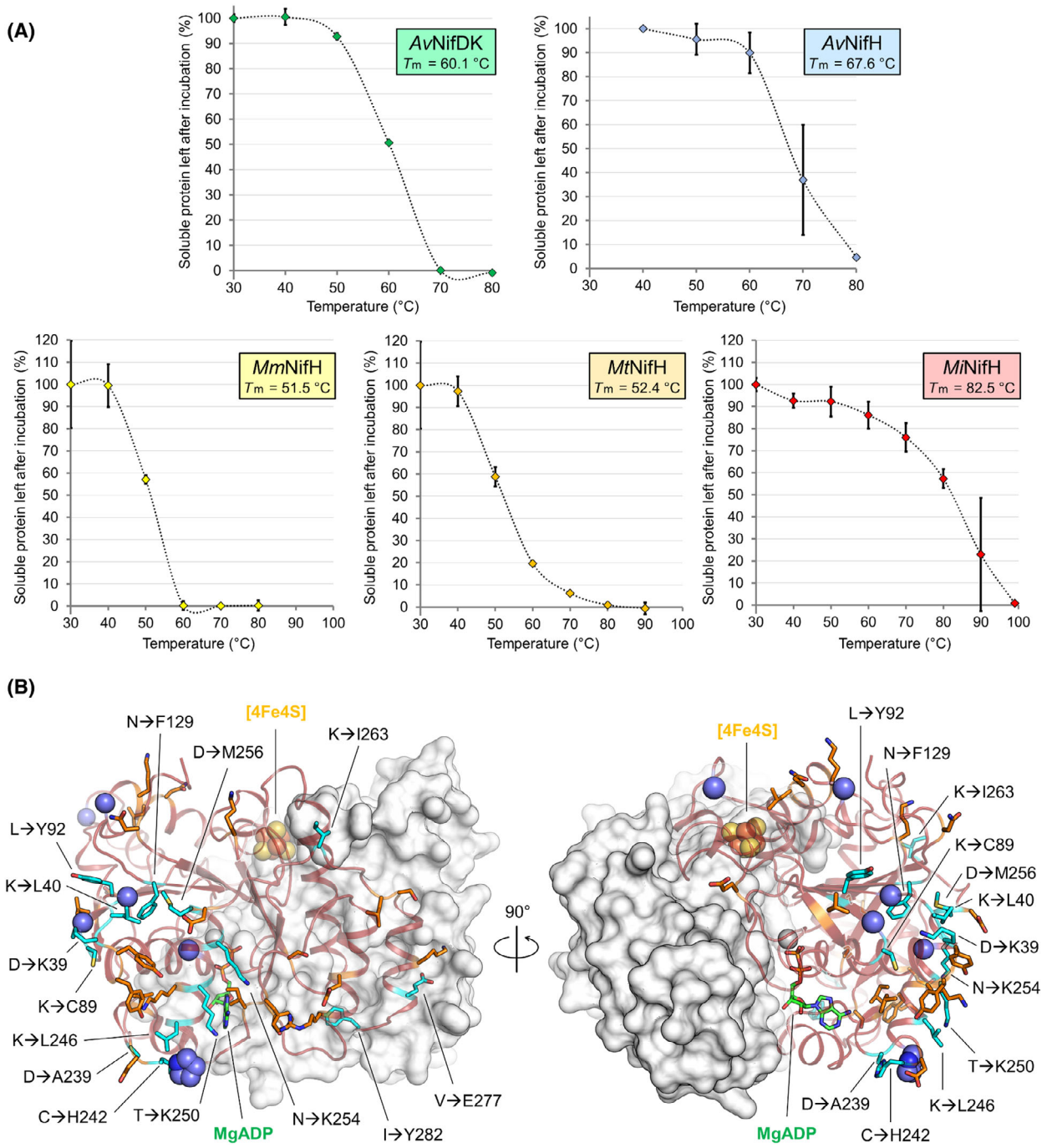

Fig. 6. Melting points of *Av*NifDK, *Av*NifH, *Mm*NifH, *Mt*NifH, *Mi*NifH and an overview of the amino acid substitutions potentially contributing to the observed differences. (A) Thermal denaturation of all proteins tested in this study following the procedure detailed in Fig. S3. The reaction volume used for incubation was 40 µL (in comparison to the one in Fig. S3, where 20 µL was used). The incubations were performed in duplicates, with the standard deviations represented as error bars for each temperature. Melting points (T_m) were estimated at 50% of the soluble protein left after 25 min of incubation. (B) Structure of *Mi*NifH with one monomer represented as a white surface and the other as a red cartoon. Sequence differences between *Mt*NifH and *Mi*NifH are highlighted by sticks, with glycine and proline displayed as spheres. Conservative and severe substitutions have carbon-coloured orange and cyan, respectively. The severe substitutions present in *Mi*NifH when compared to *Mt*NifH are labelled.

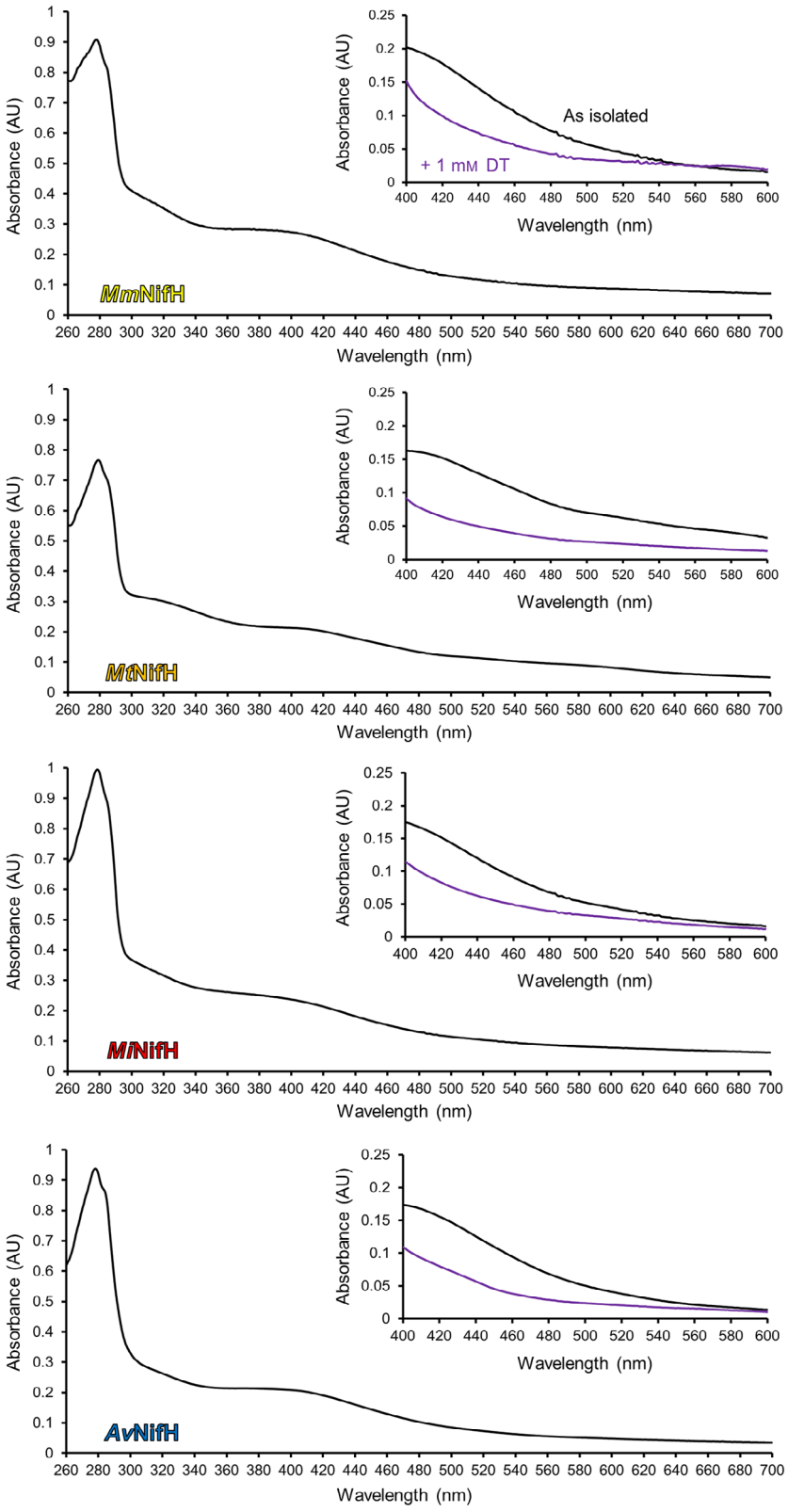

Fig. 7. UV/visible spectra of NifHs at 1 mg·mL^{-1}. The inset displays a close-up in the region of the [4Fe–4S] cluster absorption before (black line) and after 1 mM dithionite (DT) addition (purple). Absorbance values in the inlet were subtracted to the baseline measured at 700 nm.

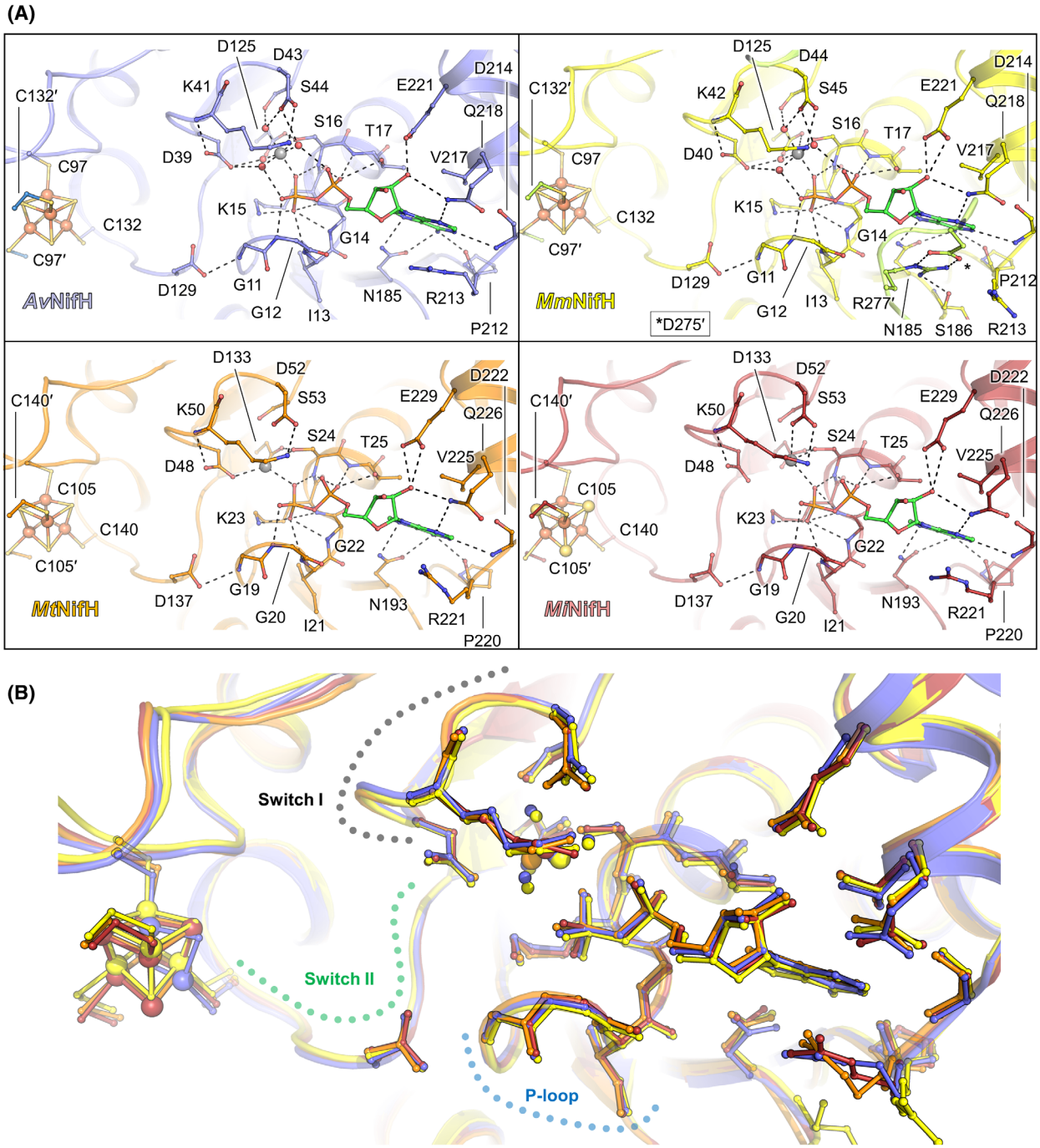

Fig. 8. (A) Conservation of the [4Fe–4S] cluster and MgADP binding site in *Av*NifH, *Mm*NifH, *Mt*NifH and *Mi*NifH. The protein is pictured in transparent cartoons on all panels (*Av*NifH, PDB: 6N4L blue, *Mm*NifH pale yellow, *Mt*NifH orange, *Mi*NifH firebrick red), with the residues coordinating the [4Fe–4S] and MgADP shown as balls and sticks. Carbon is coloured appropriately with the identity of the protein. Nitrogen, oxygen, sulphur, phosphorus, magnesium and iron are coloured blue, red, yellow, orange, grey and light orange, respectively. The primed numbers indicate the residues carried by the second monomer. (B) View of the panel's compilation in (A) with *Av*NifH (PDB: 6N4L), *Mm*NifH, *Mt*NifH, and *Mi*NifH coloured in blue, yellow, orange, and firebrick red, respectively. For clarity, the C-terminal artificial extension in *Mm*NifH, shown as lemon colour in (A), has been excluded in panel (B).

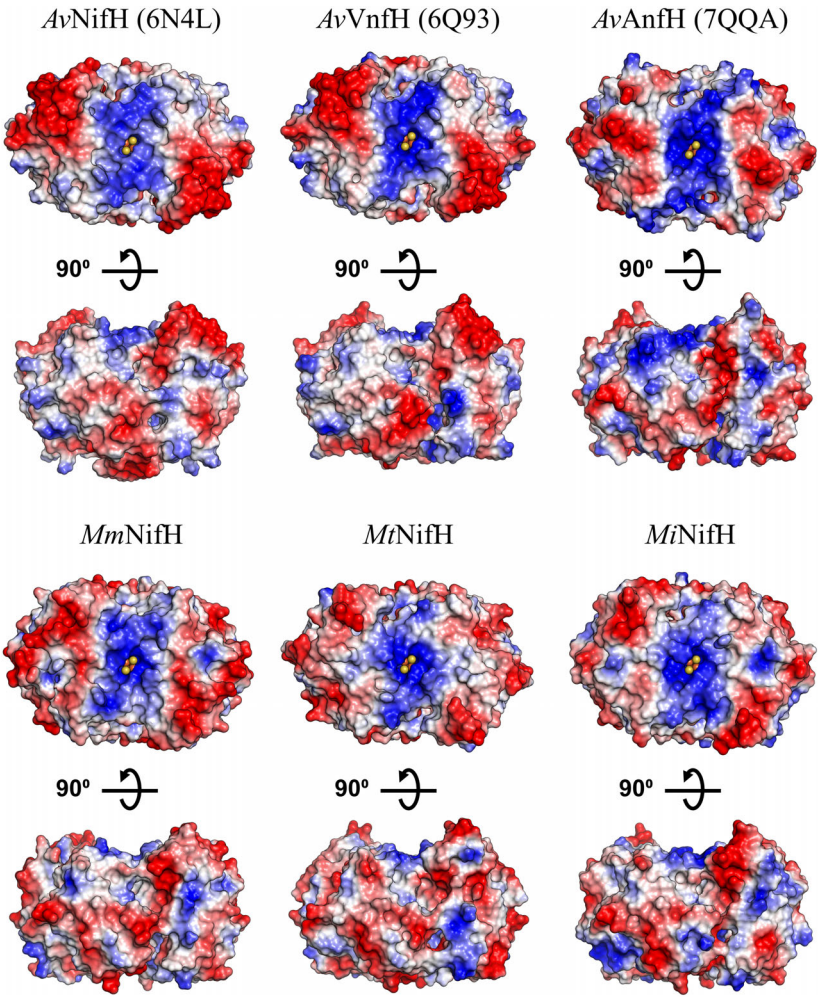

Fig. 9. Electrostatic surface properties of selected Fe proteins, all in MgADP bound state. For all models, the colour code reflects the charges on the surface from negative (red) to positive (blue). The [4Fe–4S] cluster is depicted as balls with sulphur and iron coloured in yellow and orange, respectively.

formation through migration shifts on native-PAGE as a proxy. MgADP·AlF_4^- is traditionally used as an analogue in nucleotide-switch proteins. In the nitrogenase system, it mimics the transitory state of the NifH-NifDK complex occurring during ATP hydrolysis (Fig. 1, state $3 > 4$) [66]. Once formed, the *Av*NifDKH-MgADP·AlF_4^- is considered indefinitely stable [67]. *Av*NifDK shift can be observed for all tested NifHs upon the addition of all components with some variations (Fig. 11). In the case of *Av*NifH, two bands that appeared upon complex formation were already documented in our previous work [65]. We propose that both bands might correspond to $(NifDK)_2NifH$ and $(NifDK)_2NifH_2$ population (the intermediate and top, respectively). These shifts are not dependent on $MgCl_2$, which might suggest that *Av*NifH already contains the bound cation. *Mm*NifH and *Mt*NifH exhibit similar behaviour, where the two shifted bands appear upon the complex formation (Fig. 11). However, the second band is not formed in the absence of $MgCl_2$. NifHs from *Methanococcales* locked on the bacterial nitrogenase does not reflect a physiological state that would explain the conflictual absence of activity. Even if NifHs from *Methanococcales* can bind *Av*NifDK, it does not mean that the formed complex can allow for successful electron transfer. Indeed, during the turnover, NifH dynamically changes conformations, while NifDK remains relatively static, implying the involvement of subtle rearrangement, which could be missing in this case.

Mapping of the residues involved in the NifH–NifDK interface

To deepen our investigation of the NifH–NifDK interaction, we analysed the conservation of the surface residues engaged in protein–protein contacts in the four different *Av*NifH–NifDK complexes described by Tezcan *et al.* [58]. The four snapshots were obtained with

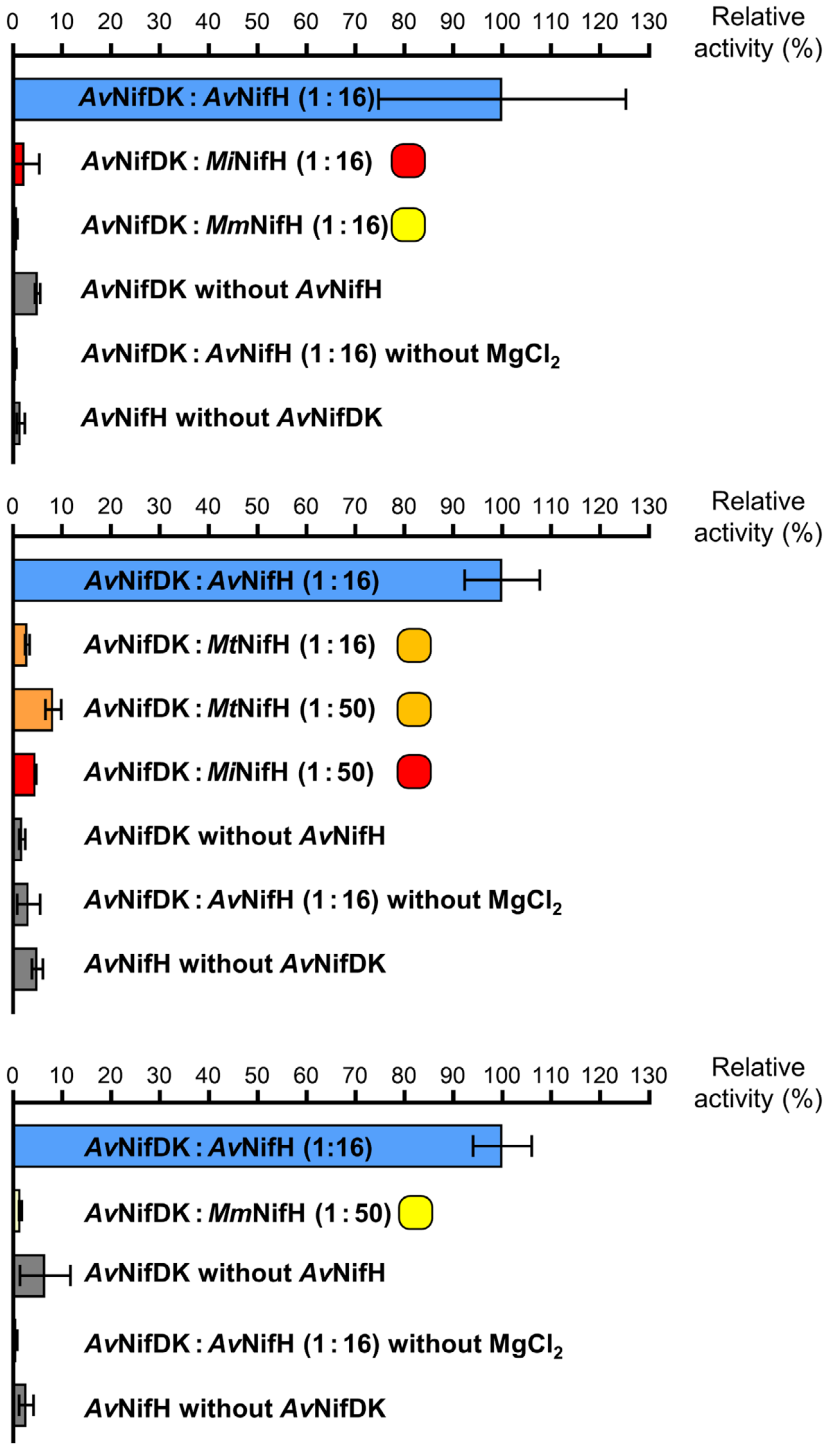

Fig. 10. Cross-reactivity of *Mm*/*Mt*/*Mi*NifH proteins with *Av*NifDK shown as a relative activity for NH_4^+ production from N_2-reduction compared to *Av*NifDKH. Relative activities for *Av*NifH, *Mm*NifH, *Mt*NifH, *Mi*NifH, and negative controls are coloured in blue, yellow, orange, red, and grey, respectively. *Mm*/*Mt*/*Mi*NifH activities are highlighted by rounded squares coloured in yellow, orange and red, respectively. *Mm*/*Mt*/*Mi*NifH do not show activity when combined with *Av*NifDK in a 1 : 16 ratio *in vitro*. Only *Mt*NifH shows a relevant activity at a ratio of 1 : 50. While the three panels represent the same type of results, they were separated according to the different experiments. All experiments have been performed in triplicates, with error bars representing the standard deviation.

the nucleotide-free, MgADP-bound, ADP·AlF_4^--bound, and MgAMPPCP-bound (mimicking the MgATP-bound *Av*NifDKH complex) states of NifH [66]. The three central residues, Arg100, Arg140 and Lys170 (numbering from *Av*NifH), interacting with NifDK in the four complexes, are all conserved in *Mm*/*Mt*/*Mi*NifHs. Gly65, making contacts with NifDK in all complexes except the nucleotide-free state, is also conserved in NifHs from *Methanococcales*. In contrast, Asn173, establishing contacts in all states except the MgAMPPCP-bound, is substituted by a glutamate. Some other charged residues involved in contacts in

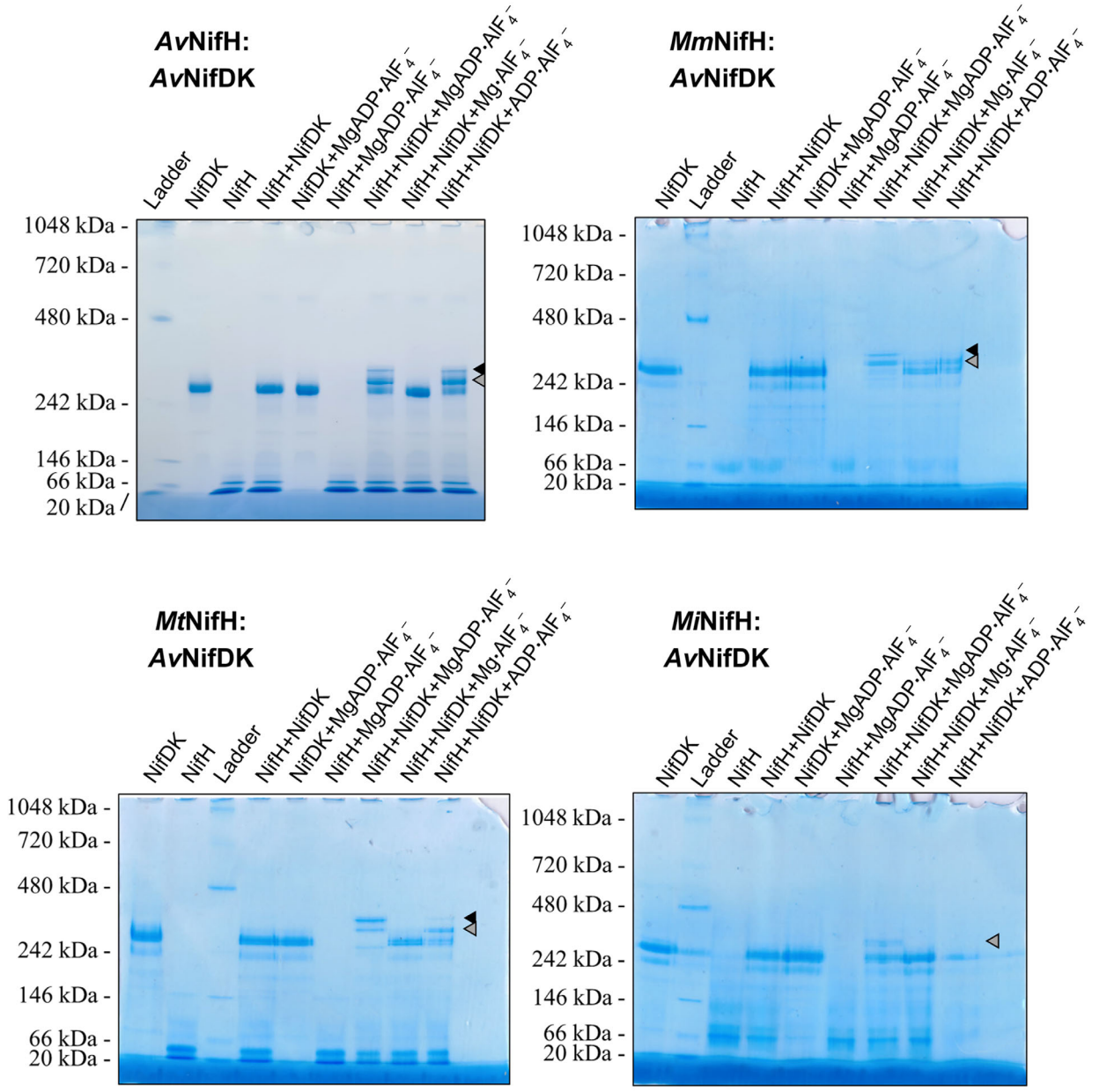

Fig. 11. Native-PAGE analysis of the recombinantly expressed NifHs from methanogens in complex with *Av*NifDK upon MgADP·AlF_4^- addition. All samples were incubated at 20 °C inside an anaerobic chamber (N_2 : H_2 97 : 3) for 1 h in 100 mM Tris/HCl pH 7.6, with 20 mM NaF, 1 mM $AlCl_3$, 1 mM ADP, and 2 mM $MgCl_2$ (when described) before loading on native PAGE. NifDK : NifH molar ratio was 1 : 5 in all cases. 3 μg of protein (for all proteins) total per well was loaded into all wells (see Materials and methods). Grey and black arrows point to the first and second shifts appearing upon complex formation, respectively.

some states are also not conserved in the three NifHs from *Methanococcales*: Glu112, Glu68, Asp69, Glu111, and Glu141. An exhaustive list of these substitutions found across *Mm*/*Mt*/*Mi*NifHs can be found in Table S2 and is illustrated in Fig. 12.

Some of these residues could impact the interaction by obstructing the optimal contact for docking and electron transfer or generating a charge repulsion that would disrupt the process.

Discussion

The importance of understanding the molecular details of nitrogenase catalysis remains of uttermost interest

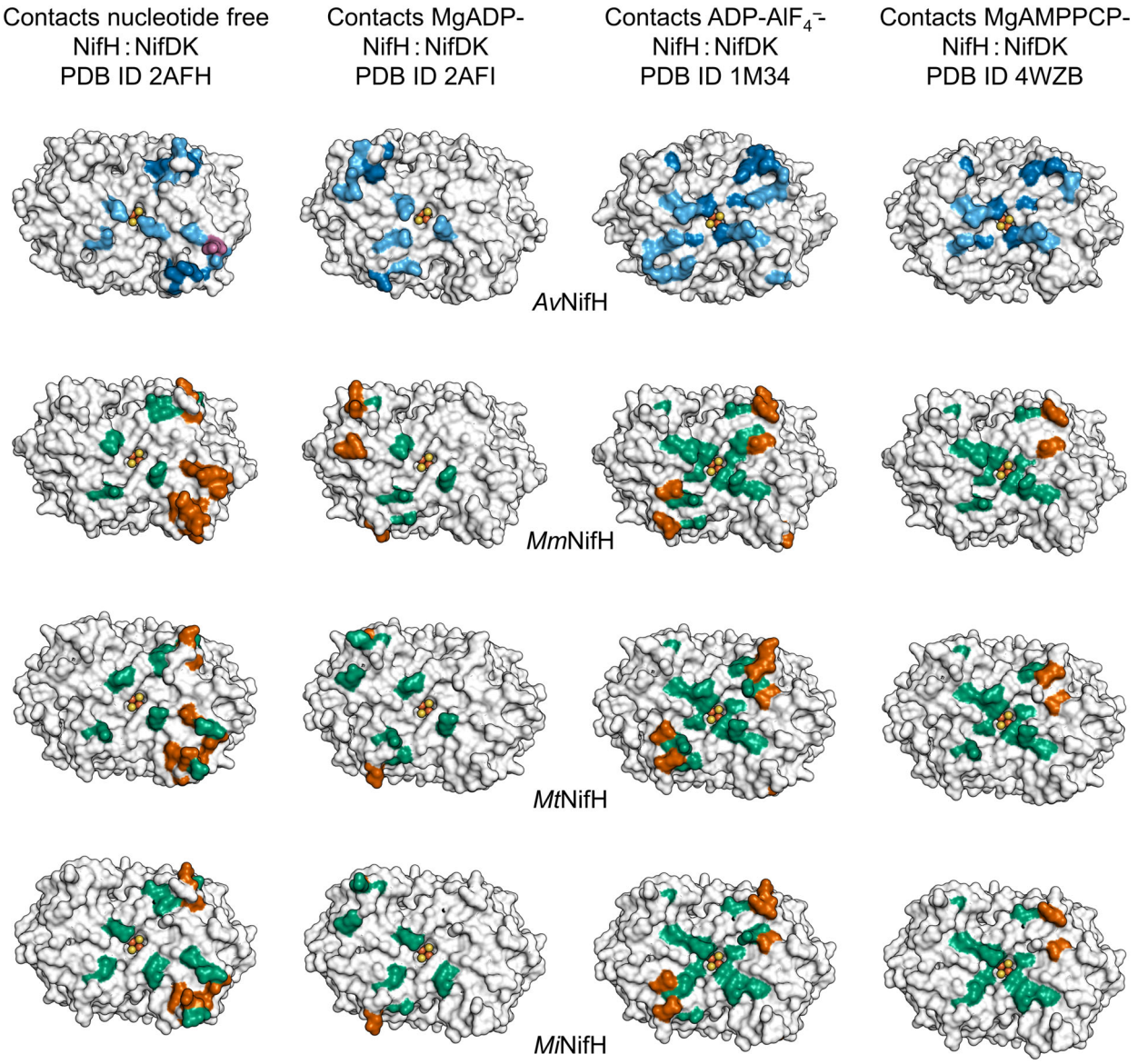

Fig. 12. Mapping of the *Av*NifH residues interacting with *Av*NifDK in four different nitrogenase complexes as described in the table S4 from Tezcan *et al.* [58]. All structures are displayed from the top view. Residues participating in the contact interface are colour coded as follows: dark blue – the contact involves the main chain atoms of a specified residue; sky blue – side chains mediate the contacts; magenta-the contact involves both the main and the side chain. For NifH from methanogens, the equivalent residues participating in the contact interface with the dinitrogenase are colour coded as follows: orange-the labelled residue is not conserved between *Av*NifH and *Mm*/*Mt*/*Mi*NifH, green-the labelled residue is conserved between *Av*NifH and *Mm*/*Mt*/*Mi*NifH. The summary of all labelled residues can be found in Table S2. The three methanogenic NifH-represented models are in the MgADP-bound state.

for agriculture [2–4], ecology [6,68], biofuel production [69,70] and evolution [15,71] alike. So far, *A. vinelandii* was the paradigm model organism for studying biological nitrogen fixation, but shifting the focus to understudied models may provide unexpectedly valuable insights. Among other candidates, methanogens stand out due to the distant phylogeny of their nitrogenases, their unique physiology and their metabolic features, which are already applied [8,53,72,73]. These archaea possibly play important roles in marine environments where they could contribute to the nitrogen input for the microbial community [47–50]. On the way to an in-depth understanding of the nitrogen fixation in these peculiar microorganisms, we elucidated the first component of their machinery. We obtained the first X-ray crystal structures of NifHs from a thermophile

and hyperthermophile by directly purifying the enzymes from the organisms.

Methanococcales as (hyper)thermophilic species are particularly interesting models to investigate nitrogen fixation under high temperatures [52]. This is illustrated by the remarkable thermostability of *Mi*NifH in which a dozen of substitutions seem to be enough to increase the T_m for 30 °C compared to *Mt*NifH homologue (Fig. 6). Additional cellular factors (e.g., osmolytes, high potassium phosphate concentration) might also contribute to NifH thermostability *in vivo*. Still, our study already highlights the potential of the *M. infernus* system for possible biotechnological applications.

The performed structural analyses confirm that all Fe proteins so far share the same architecture and harbour the conserved key elements of the functional P-loop NTPases: the P-loop, the switch I and switch II. Strikingly, despite their extremely high three-dimensional conservation with *Av*NifH, and our efforts, we could not detect relevant NH_4^+-production when *Mm*/*Mt*/*Mi*NifHs are combined with *Av*NifDK in a cross-reactivity assay. This echoes the work of Jasper *et al.* [64], in which the reductases from the chlorophyll and cofactor F_{430} biosynthesis could bind the bacterial nitrogenase to some extent but did not support the N_2-reduction. The N_2-reduction reaction between cross-kingdom proteins is possible [63], as it has been shown that the recombinant *Ma*NifH and *Ma*VnfH can electronically fuel *Av*NifDK, albeit with lower rates compared to the native system (11% and 36% relative activity, respectively). One reason for the lack of observed activities might be the slow electron transfer rate, favouring metal-hydride protonolysis (parasitic H_2 production) and rendering N_2-fixation inefficient. This should be verified in the future by quantification of the produced H_2 along with the NH_4^+ quantification. The temperature of 30 °C at which the assay was carried out and the discrepancy between the expected optimum of 65 and 85 °C for *Mt*NifH and *Mi*NifH, respectively, might also drastically influence the dynamic and electron transfer rate. Still, it does not explain the lack of activity for *Mm*NifH. Another plausible explanation is the differences in terms of contacts. Available data on the cross-reactivity of the three Fe proteins from *A. vinelandii* [38] and the one from *M. acetivorans* [63], and this study shows a lack of correlation between the sequence identity and the production of NH_4^+ between the hybrid systems. This is exemplified when considering the cross-over between the three Fe protein isoforms and the three different dinitrogenase isoforms [38]. Since genetic systems exist in the mesophiles *A. vinelandii* and *M. maripaludis*, it would be interesting to determine whether diazotrophic growth can physiologically occur with hybrid systems.

Cross-reactivity assays provide additional insights for understanding and modelling binding mechanistic, ATP-consumption rates, electron-transfer efficiencies and engineering of nitrogenases to capture targeted substrates and intermediates. The substitutions listed in Table S2 also suggest the existence of an adaptation on the surface of the nitrogenase from *Methanococcales*. While it is expected that the analogous binding interface should, in principle, reflect a similar mechanism, some rearrangement might have occurred due to additional partners present in *Methanococcales*. For instance, Leigh' s work highlighted how the $NifI_{1,2}$ couple, belonging to the P_{II} superfamily of regulatory proteins, interferes with NifH binding efficiency [74,75]. Such a post-translational regulation system might require changes in the dinitrogenase surface and, as a response, the observed substitutions in *Mm*/*Mt*/*Mi*NifHs. Structural insights into the whole nitrogenase complex from these ancient microorganisms will unveil its unique features, but more importantly, it could be used as a new model to deepen our knowledge of biological N_2-fixation.

Materials and methods

M. thermolithotrophicus growth conditions

Both *Mt*NifH without ligands and with bound MgADP were obtained from derepressed *M. thermolithotrophicus* cells. *M. thermolithotrophicus* strain DSM 2095 (Leibniz Institute DSMZ – German Collection of Microorganisms and Cell Cultures, Braunschweig, Germany) was cultivated anaerobically on 10 mM NH_4Cl with a gas phase of 1 bar H_2/CO_2 in 5 L safety-coated Duran bottles, standing at 37 °C. Each bottle contained 300 mL of medium, with a 1 : 10 inoculum. As the inoculum, adapted diazotrophic cells, grown as described in Maslać *et al.* [42], were used. After 48 h of incubation, cells were transferred in an anaerobic tent (atmosphere containing a mixture of N_2/CO_2 at a 90 : 10% ratio) and harvested anaerobically at 6000 ***g*** for 30 min at room temperature. The pellet was washed with the same medium without NH_4Cl. The centrifugation step was repeated as described. Finally, the pellet was resuspended in the final volume of 600 mL NH_4Cl free medium and transferred to 2 L safety-coated Duran bottles, each containing 150 mL of culture.

Prior to the transfer, the gas phase in the bottles was exchanged in 5 cycles of vacuuming to −1 bar and gassing with N_2 (the first 3 cycles) or H_2/CO_2 (the last 2 cycles) to +1 bar. The gas phase finally contained +1.6 bar H_2/CO_2 total (added after the final cycle of vacuuming to −1 bar) and an additional 0.6 bar N_2. Resuspended cells were incubated for 24 h, standing at 37 °C. Harvesting was done by centrifugation at 6000 ***g*** for 30 min at room temperature. In

both cases, the pellets were flash-frozen in liquid nitrogen and stored at −80 °C before use. The medium was prepared as described in Maslać *et al.* [42], with the addition of 10 mM NH_4Cl in the case of NH_4Cl-containing medium.

Purification of native *Mt*NifH from *M. thermolithotrophicus* cells

Cell pellets of *M. thermolithotrophicus* were (~4 g of wet cells from the 1.5 L of total culture for NifH without ligands and ~16 g of wet cells from the 6.5 L of total culture for NifH with bound MgADP) thawed at room temperature and sonicated inside an anaerobic chamber (N_2/CO_2 (90 : 10%) atmosphere) after being diluted with ion exchange buffer (IEX buffer; 50 mM Tris/HCl pH 8.0 and 2 mM dithiothreitol (DTT)). Sonication was done in the same anaerobic chamber (KE76 probe Bandelin SONOPULS, Sigma, Berlin, Germany) at 70–75% intensity (10 times for 10 s). The lysate was centrifuged at 35 000 ***g*** for 30 min at 18 °C in the case of the first batch and at 75 600 ***g*** for 1 h at 18 °C in the case of the NifH with bound MgADP and transferred to an anaerobic Coy tent (N_2/H_2 (97 : 3%) atmosphere). All the following steps have been done at 20 °C and under yellow light. The supernatant was filtered through a 0.2 µm filter (Sartorius, Göttingen, Germany) and loaded on a 20 mL HiTrap DEAE Sepharose Fast Flow column (Cytiva, Freiburg, Germany) previously equilibrated with IEX Buffer. Elution was done with a 0–500 mM NaCl linear gradient for 18 column volumes (CVs) at a 3 mL·min^{-1} flow rate. The fractions containing *Mt*NifH were obtained between 301 and 350 mM NaCl. The fractions of interest were pooled together and loaded on a 10 mL HiTrap Q-Sepharose High-Performance column (GE Healthcare Life Sciences, Munich, Germany) after being filtered. Elution from Q-Sepharose was performed by applying a 400–600 mM NaCl linear gradient (with the same IEX buffer above with 50 mM Tris/HCl at pH 9.0) for 9 CVs at a 1.5 mL·min^{-1} flow rate. *Mt*NifH eluted in fractions between 418 and 450 mM NaCl. Fractions were pooled, diluted 1 : 3 (pool : buffer) with hydrophobic exchange buffer (HIC; 25 mM Tris/HCl pH 7.6, 2 M $(NH_4)_2SO_4$ and 2 mM DTT) and filtered before being injected on a 5 mL Phenyl Sepharose High-Performance column (GE Healthcare Life Sciences). Under this condition, *Mt*NifH was not binding to the column and was collected in the flow through. The final yield of the purification was 0.66 mg of *Mt*NifH from the first batch and 8.19 mg *Mt*NifH from the second batch.

Methanocaldococcus infernus growth conditions

Methanocaldococcus infernus strain DSM 11812 (Leibniz Institute DSMZ – German Collection of Microorganisms and Cell Cultures, Braunschweig, Germany) was adapted to the diazotrophic condition and grown in a medium similar to the one described in Maslać *et al.* [42] with the following modification of the growth medium: instead of Na_2SeO_4, $Na_2SeO_3{\cdot}5H_2O$ was used as a final concentration of 2 µM; the concentration of $Na_2WO_4{\cdot}H_2O$ was increased to 100 µM, and the medium contained Na_2SO_4 at the final concentration of 10 mM. The final pH of the medium was adjusted to 6.5 aerobically before switching it to anaerobic conditions, as described in Maslać *et al.* [42]. The cells were cultivated in 1 L pressure-resistant Duran bottles containing 60 mL of medium with a gas phase of +1.5 bar H_2/CO_2 and an additional 0.5 bar N_2 (added after the final cycle of vacuuming to −1 bar while exchanging the gas phase in the bottles as described above) and standing at 75 °C. Cultures were inoculated 1 : 20 using diazotrophic *M. infernus* cells as an inoculum. The cells were harvested and stored as described for *M. thermolithotrophicus* cells above.

Purification of native *Mi*NifH

Methanocaldococcus infernus cells (~25.62 g wet cells obtained from 5.5 L of culture) were thawed and sonicated as described above, using the same IEX buffer. The cell lysate was centrifuged anaerobically at 45 000 ***g*** for 1 h at room temperature. Purification was done inside an anaerobic chamber with N_2/H_2 (97 : 3%) atmosphere at 20 °C and under yellow light. The filtered supernatant was loaded on a 10 mL HiTrap Q-Sepharose High-Performance column (GE Healthcare Life Sciences) and eluted with a 250–700 mM NaCl linear gradient for 4.5 CVs at a 1.5 mL·min^{-1} flow rate.

The fractions containing *Mi*NifH obtained between 314 and 407 mM NaCl were pooled and diluted 1 : 2.5 (pool : buffer) with HIC buffer, filtered as described above, and loaded on a 5 mL Phenyl Sepharose column (GE Healthcare Life Sciences). Elution was done with a 1.9–0.6 M $(NH_4)_2SO_4$ linear gradient for 13 CVs at a 1 mL·min^{-1} flow rate. *Mi*NifH was obtained between 0.943 and 0.726 M $(NH_4)_2SO_4$. The final yield of the purification was 3.12 mg.

Escherichia coli strains and plasmids used to produce recombinant NifH proteins

In this study, three different *E. coli* strains were used (Table S3): (a) *E. coli* DH5α carrying WG35 vector with *M. maripaludis* NifH (cloned from *M. maripaludis* strain S2-derivative MM901, J. Leigh [76]) (b) *E. coli* BL21 Δ*iscR* (provided by J. Swartz, Department of Chemical Engineering (Stanford University, Stanford, USA)) and (c) *E. coli* DH5α carrying pDB1282 plasmid (original construct from D. Dean, Department of Biochemistry, Virginia Tech, Blacksburg, USA).

Synthetic gene constructs

*Mt*NifH and *Mi*NifH sequences (see the Supporting Information) were codon optimised for *E. coli*, synthesised and cloned into pET-28(+) vectors using the restriction sites NcoI and NdeI. A linker followed by a thrombin cleavage site, a His-tag and the stop codon was inserted at the end of the synthetic gene before the NdeI cleavage site (see the Supporting Information). All these steps were performed by GENSCRIPT (GenScript Corp, Piscataway, NJ, USA).

Growth conditions of *E. coli* BL21 Δ*iscR* WG35 (for *Mm*NifH) and cell harvesting

Escherichia coli BL21 Δ*iscR* transformed with plasmid WG35 was grown in an 8 L fermenter in Terrific Broth medium (per litre 12 g of tryptone, 24 g of yeast extract, 5 g of glycerol, 1 : 10 diluted TB salts (2.32 g·L^{-1} KH_2PO_4 and 12.54 g·L^{-1} K_2HPO_4 final)) containing 10 mM MOPS buffer pH 7.4, 2 mM ferric ammonium citrate, 27.75 mM glucose, 50 µg·mL^{-1} kanamycin and 100 µg·mL^{-1} ampicillin. The cells were incubated at 37 °C until they reached an OD_{600nm} of 1.3. Here, the temperature was decreased to room temperature, and the fermenter switched to anaerobic condition by sparging with 100% N_2. The cells were induced immediately after equilibration by adding IPTG (0.5 mM final), fumarate (25 mM final) and cysteine (2 mM final). After overnight expression, the cells were harvested anaerobically by centrifugation for 15 min at 17 700 ***g*** at 10 °C. The cell pellet was washed with anaerobic phosphate-buffered saline (PBS, 140 mM NaCl, 2.7 mM KCl, 10 mM Na_2HPO_4, 1.8 mM KH_2PO_4) inside an anaerobic chamber (N_2/CO_2 (90 : 10%) atmosphere) before being pelleted again as described above. The pellets were flash-frozen in liquid nitrogen and stored anaerobically at −80 °C until use.

Growth conditions of *E. coli* BL21 pDB1282 pET-28(+) *Mt*/*Mi*NifH and cell harvesting

Escherichia coli BL21 carrying plasmids pDB1282 pET-28 (+) *Mt*/*Mi*NifH cells were grown in 1 L Duran flasks containing 0.33 L of the medium. The medium composition and the growth conditions were the same as described above for *E. coli* BL21 Δ*iscR* WG35 cells. The culture was grown aerobically at 37 °C, shaking at 180 r.p.m. until an $OD_{550\ nm}$ of 0.5 was reached. Upon reaching this OD, the headspace was exchanged to 100% N_2 by aseptic flushing using the Hungate technique and the bottles were sealed with sterile gas-tight rubber stoppers and caps. To induce the cells, anaerobic IPTG (250 µM final), fumarate (25 mM final), cysteine (2 mM final) and 0.2% w/v L-arabinose were added by sterile filtration. The cultures were further incubated at 25 °C and shaking at 180 r.p.m. overnight. The cells were harvested anaerobically by centrifugation for 15 min at 17 700 ***g*** at 10 °C, washed with anaerobic PBS, pelleted again, flash frozen in liquid nitrogen and stored anaerobically at −80 °C until use.

Purification of recombinant NifH proteins

In all cases, the respective cell pellets of transformed cells were thawed on ice and resuspended in an anaerobic Lysis Buffer (50 mM $Na_2HPO_4{\cdot}2H_2O$, 500 mM NaCl, 20 mM imidazole, 5% glycerol, adjusted to pH 8.0 with HCl) inside of an anaerobic chamber (N_2/CO_2 (90 : 10%) atmosphere). Sonication was done in the same anaerobic chamber (KE76 probe Bandelin SONOPULS, Sigma) at 75% intensity (30 times, 10 s).

The cell lysate was centrifuged at 20 442 ***g*** for 45 min at 4 °C to remove cell debris and unbroken cells. The supernatant (soluble fraction) was transferred to an anaerobic tent (N_2/H_2 (97 : 3%) atmosphere), filtered through a 0.2 µm filter (Sartorius), and loaded on 10 mL His-Trap nitrilotriacetic acid column loaded with Nickel (Ni-NTA, GE Healthcare Life Sciences). The column was previously washed and equilibrated with the Lysis Buffer.

Elution was done with a 20–320 mM imidazole linear gradient for 6 CVs at a 1 mL·min^{-1} flow rate in all cases. *Mm*NifH was eluted between 170 and 257 mM imidazole, *Mt*NifH was eluted between 246 and 283 mM imidazole, and *Mi*NifH was eluted between 205 and 257 mM imidazole.

Based on SDS/PAGE and the brown colour of the different fractions, the purest fractions were pooled together and diluted with 3 volumes of IEX buffer, filtered, and loaded on a 10 mL HiTrap Q-Sepharose High-Performance column (GE Healthcare Life Sciences). Elution was done using a 0–800 mM NaCl linear gradient for 6 CVs at a 1 mL·min^{-1} flow rate. The fractions containing *Mm*NifH were obtained between 506 and 614 mM NaCl, *Mt*NifH was eluted between 455 and 561 mM NaCl, while *Mi*NifH was eluted between 401 and 547 mM NaCl. The final yield of the purification was 6.0, 13.4, and 32.4 mg for *Mm*NifH, *Mt*NifH and *Mi*NifH, respectively.

Crystallisation

All samples were concentrated with a 10-kDa cutoff with VivaSpin amicons (Sartorius) to the desired concentration. All samples were crystallised inside an anaerobic chamber (N_2/H_2 (97 : 3%) atmosphere, 20 °C). Prior to crystallisation, samples were centrifuged at 13 000 ***g*** for 3 min to remove macro-aggregates and dust. When the proteins were co-crystallised with ligands, the ligands were mixed with the sample before the centrifugation step. The crystallisation was done in 96-Well MRC 2-Drop polystyrene plates (SWISSCI) containing 90 µL of crystallisation solution in the reservoir in all cases.

*Mm*NifH was crystallised at a final concentration of 13 mg·mL^{-1} with 2 mM ATP and 2 mM $MgCl_2$ by mixing

0.7 µL of crystallisation solution with 0.7 µL of protein sample. Crystals were obtained in 20% w/v polyethylene glycol 3000, 100 mM Tris pH 7.0 and 200 mM calcium acetate and were soaked in the crystallisation solution supplemented with 20% glycerol prior to freezing in liquid nitrogen. Despite the addition of ATP, only ADP could be observed in the electron density, probably due to hydrolysis over time.

*Mt*NifH nucleotide-free was crystallised at a final concentration of 6 mg·mL^{-1} by spotting 0.5 µL of crystallisation solution with 0.5 µL of protein sample. The crystallisation solution contained 30% v/v 2-methyl-2,4-pentanediol, 100 mM sodium acetate, pH 4.6 and 20 mM calcium chloride. *Mt*NifH with ligands was crystallised at a final concentration of 32.7 mg·mL^{-1}, with 10 mM ATP and 10 mM $MgCl_2$ by spotting 0.5 µL of crystallisation solution (20% w/v polyethylene glycol 8000, 100 mM Tris, pH 8.5 and 200 mM magnesium chloride) with 0.5 µL of the protein sample. Obtained crystals of *Mt*NifH with ligands were soaked in the crystallisation solution supplemented with 30% glycerol prior to freezing in liquid nitrogen.

*Mi*NifH was crystallised at a final concentration of 18.3 mg·mL^{-1}, with 2 mM ADP and 2 mM $MgCl_2$, by spotting 0.7 µL of crystallisation solution with 0.7 µL of protein sample. In this case, the crystallisation solution contained 20% w/v polyethylene glycol 3350, 100 mM Bis-Tris propane pH 8.5 and 200 mM sodium nitrate and crystals were soaked in the crystallisation solution supplemented with 20% ethylene glycol prior to freezing in liquid nitrogen. Sealed plates were stored inside the same anaerobic chamber where the crystallisation was performed.

Data collection, integration, scaling, model building and refinement

Data were collected at Synchrotron SOLEIL French National Synchrotron Facility (Paris, France, beamline Proxima I) and the Swiss Light Source Synchrotron (Villigen, Switzerland, beamlines PXI and PXIII) (see Table 1) and were integrated with *autoPROC* [77]. All datasets were treated with Staraniso except for *Mt*NifH nucleotide-free forms, which did not exhibit anisotropy [78]. *Mt*NifH nucleotide-free form 2 was solved by molecular replacement with the nucleotide-free model from *Av*NifH (PDB code 2NIP). All *Mt*NifH models were solved by molecular replacement with *Mt*NifH nucleotide-free form 2 as a template. *Mm*NifH and *Mi*NifH structures were solved by molecular replacement with the *Mt*NifH-MgADP complex. All molecular replacements were done with PHASER [79] from the PHENIX SUITE [80]. All models were manually optimised with COOT [81]. Refinement was performed with PHENIX without applying non-crystallography symmetry. Translation-libration screw was used during refinement. *Mm*NifH suffered from a pseudo-merohedral twinning with a calculated twin fraction of 0.15, and the refinement was performed by imposing the following twin law: *h*, *-k*, *-l*. With the exception of *Mt*NifH with ligands, all models were refined with riding hydrogens that were omitted in the final deposited models. All structures were validated by the Molprobity server [82] (on the 15th of April, 2023). All presented figures containing protein structures were generated using PYMOL MOLECULAR GRAPHICS SYSTEM, Version 2.2.0 Schrödinger, LLC (New York, NY, USA).

Azotobacter vinelandii growth conditions: medium composition

Azotobacter vinelandii RS1 (derived from strain DJ) [65,83] preculture was grown in a 250 mL baffled culture flask (glass) with a vented cap containing 120 mL of sterile liquid media (modified Burke's medium). Each preculture was started by inoculation from a fresh agar plate and grown aerobically at 200 r.p.m. at 30 °C until $OD_{600\ nm} > 2.0$ (usually overnight).

Under sterile conditions, the preculture was used at a 1 : 10 ratio to inoculate the 12 L of liquid media dispatched in 4 × 5 L baffled flasks (Corning CLS431684, 3 L of culture per bottle) with vented caps. Cells were grown at 200 r.p.m. at 30 °C overnight until an $OD_{600\ nm} > 1.5$ was reached. Cells were collected by serial centrifugation runs at 4500 ***g***, 15 min at room temperature. The supernatant was discarded, and the cells were gently resuspended in a fresh growth medium devoid of NH_4OAc or another source of fixed nitrogen (prepared fresh but not under sterile conditions) in the incubator shaker (~ 400 mL media per bottle). After resuspension, the culture was divided evenly between the remaining media/bottles and incubated at 200 r.p.m. and 30 °C for another 3 h to facilitate derepression of the *nif* operon. Cells were harvested by serial centrifugation collections as above. Finally, the cells were scooped into a plastic bag and stored at −80 °C until further use. Modified Burke's medium was prepared by adding 120 mL of an autoclaved 100 × phosphate buffer solution (0.46 M K_2HPO_4, 0.15 M KH_2PO_4), 40 mL of a filter-sterilised 3 M NH_4OAc solution, 12 mL of a filter-sterilised 0.1 M Fe solution ($FeCl_3{\cdot}6H_2O$) and 12 mL of a filter-sterilised 10 mM Mo solution ($Na_2MoO_4{\cdot}2H_2O$) to 12 L of autoclaved salt medium (60 mM sucrose, 8.1 mM $MgSO_4{\cdot}7H_2O$, 6.1 mM $CaCl_2$), all at room temperature, under sterile conditions. All buffers and solutions were prepared with MilliQ water (18.2 MΩ cm). Generally, large volumes (> 50 mL) were sterilised by autoclaving; smaller solutions were sterilised by filtration (0.45 µm syringe filters).

*Av*NifDK and *Av*NifH purification

Cell pellet (~ 77 g) was anaerobically thawed and resuspended for 45 min in lysis buffer (50 mM Tris/HCl pH 8.0, 5 mM dithionite, 37% v/v glycerol) with a 2 : 1 ratio (buffer: cells v/w) inside a Coy anaerobic chamber (N_2 : H_2 95 : 5,

Coy Laboratory Products, Grass Lake, MI, USA). Treated cells were collected by centrifugation at 12 000 ***g*** for 25 min at 4 °C in deoxygenated and anoxically sealed poly(propylene) bottles. The cell pellet was resuspended in 200 mL of glycerol-free lysis buffer (containing a few µg of DNase) and lysed by osmotic shock/shaking. Lysed cells were incubated on ice for 20 min and pelleted by anaerobic centrifugation at 26 000 ***g*** at 4 °C for 1 h. The obtained supernatant was mixed with 20 mL of post-lysis buffer (2 M NaCl, 234 mM Tris, pH 8.0) and loaded on a 20 mL His Prep FF 16/10 column equilibrated with chelating equilibrating buffer (50 mM Tris/HCl, 300 mM NaCl, pH 8.0). The flow-through containing the *Av*NifH was collected. The elution was done with chelating elution buffer (50 mM Tris, 300 mM NaCl, 300 mM imidazole, pH 8.0) in two steps. The first step containing 20 mM imidazole was used to remove weakly bound proteins, and the second at 300 mM imidazole step was to elute *Av*NifDK.

Collected *Av*NifDK was diluted 1 : 3 (v/v) with 50 mM Tris/HCl pH 8.0 and 5 mM EDTA-disodium salt and loaded on a 20 mL Q Sepharose HiPrep HP 16/10 column equilibrated with ion exchange buffer A (50 mM Tris/HCl pH 8.0). The elution was done with ion exchange buffer B (50 mM Tris/HCl, 1 M NaCl, pH 8.0) in two steps: 100 mM NaCl washing step and 1 M NaCl step to elute *Av*NifDK.

*Av*NifH was diluted and loaded on a 20 mL Q Sepharose HiPrep HP 16/10 column, the same way as described above for *Av*NifDK and eluted with 200–650 mM linear NaCl gradient over 7 column volumes. Fractions containing *Av*NifH were determined based on SDS/PAGE, pooled together and concentrated before loading on a Sephacryl S-200-HR HiPrep 26/60 320 mL column.

Both samples were concentrated using a Merck Millipore (Darmstadt, Germany) stirred concentrator cell equipped with a 100 (for *Av*NifDK) or 30 kDa (for *Av*NifH) molecular weight cut-off membrane (fed with ultra-high-purity N_2 5.0) and flash frozen in liquid nitrogen as 20 µL pellets and stored in liquid nitrogen until further use. The final yield of the purification was 109.25 mg for the *Av*NifH and 370.37 mg for the *Av*NifDK.

Thermal denaturation experiment

The following experiment was performed in duplicate in a Coy anaerobic chamber (N_2/H_2 97 : 3, 20 °C, Coy Laboratory Products). Proteins were diluted to a final concentration of 5 mg·mL^{-1} in 50 mM Tris pH 8.0, 100 mM NaCl, and 2 mM DTT in 40 µL (or 20 µL for Fig. S3). Eppendorf tubes containing the protein were transferred to a block heater at the temperature described in Fig. 6 and Fig. S3 and incubated for 25 min. Following the incubation, the tubes were immediately centrifuged at 20 °C for 25 min at 6000 ***g***. 10 µL (or 5 µL for Fig. S3) of each supernatant was diluted 10 times with 50 mM Tris pH 8.0 and 2 mM DTT before protein quantification by the Bradford method. Protein quantification was performed aerobically. The values reported in the graphs of Fig. 6 and Fig. S3 correspond to the protein quantification ratios of the supernatants after and before heat treatment.

UV-visible spectrophotometry

The UV-visible spectrophotometric profile of each NifH was taken anaerobically (in an atmosphere containing 97% N_2 and 3% H_2) with a final protein concentration of 1 mg·mL^{-1} in 50 mM Tris/HCl pH 8.0 and 2 mM DTT. The samples were transferred in a 1-cm path quartz cuvette and measured at room temperature on a Cary 60 (Agilent Technologies, Waldbronn, Germany).

The estimation of the [4Fe–4S] cluster occupancy was based on the protein concentration obtained by Bradford measurement and by approximating the extinction coefficient for [4Fe–4S] clusters to $\varepsilon_{410} = 15\ \text{mM}^{-1}\cdot\text{cm}^{-1}$ [62]. The calculation took into account 2 mol of NifH for 1 mol of [4Fe–4S] (i.e., the molecular weight of tagged *Mm*NifH, tagged *Mt*NifH, tagged *Mi*NifH, and native *Av*NifH being 63 416, 66 378, 66 010 and 63 032 g·mol^{-1}). The [4Fe–4S] cluster occupancy has not been given for *Av*NifH (calculated to 70%) in the main text since the stock of frozen protein was conserved in 2 mM dithionite (e.g., a part of the population might be in the reduced state). In comparison, the three NifHs from *Methanococcales* were principally isolated in the oxidised state. The reduced states were obtained by adding a final concentration of 1 mM dithionite to the protein (from a 100 mM solution of freshly prepared dithionite) and measured under the same conditions.

Activity assays

Activity assays were performed in triplicate and contained a final volume of 1 mL per reaction. The reactions were performed in 13 mL septum-sealed glass vials (Wheaton) in deoxygenated buffer containing an ATP-regenerating system (5 mM ATP, 30 mM phosphocreatine, 0.6 mg·mL^{-1} bovine serum albumin, 200 µg·mL^{-1} creatine phosphokinase (from Rabbit muscle, Merck/Roche, Darmstadt, Germany), 10 mM sodium dithionite and 100 mM MOPS/NaOH at pH 7.0). All reactions contained 0.1 mg of *Av*NifDK and 16.6 or 50 molar equivalents of NifH (corresponding to 0.5 and 1.56 mg, respectively). All reaction vials were prepared and sealed inside an anaerobic chamber under a 100% N_2 atmosphere and vented to atmospheric pressure before starting the reaction. Reactions were performed within a standing water bath (30 °C) and initiated by adding $MgCl_2$ (from a 1 M stock, 10 mM final concentration). After 8 min, the reactions were quenched by adding 300 µL of 400 mM EDTA (pH 8.0). NH_4^+ was quantified by the *ortho*-phthalaldehyde method using NH_4Cl as the standard, as reported previously [84–86].

High-resolution clear native PAGE (hrCN PAGE) and MgADP·AlF_4^- stabilisation

To test the formation of MgADP·AlF_4^--stabilised NifDK-NifH complexes, all samples were incubated at 20 °C inside an anaerobic chamber (N_2 : H_2 97 : 3) for 1 h in 100 mM Tris/HCl pH 7.6, with 20 mM NaF, 1 mM $AlCl_3$, 1 mM ADP and 2 mM $MgCl_2$ before loading on hrCN PAGE. In all cases, NifDK and NifH were mixed in a molar ratio of 1 : 5 (corresponding to 45 µg of NifDK and 67.5 µg of NifH), and the mixture was diluted to a final concentration of 0.6 mg·mL^{-1} prior to the loading on the gel, in the corresponding buffer. The 3–15% linear polyacrylamide gradient hrCN PAGE was run in the same anaerobic chamber and prepared according to Lemaire *et al.* [87]. Cathode buffer contained 50 mM Tricine, 15 mM Bis-Tris/HCl, pH 7.0, 0.05% (w/v) sodium deoxycholate, 2 mM DTT and 0.01% (w/v) dodecyl maltoside, while the anode buffer contained 50 mM bis–tris/HCl buffer pH 7.0 and 2 mM DTT. Electrophoresis was run with a constant 40 mA current (PowerPacTM Basic Power Supply, Bio-Rad, Feldkirchen, Germany). Protein bands were visualised with Ready BlueTM Protein Gel stain (Sigma Aldrich, Hamburg, Germany). NativeMark™ Unstained Protein Standard (ThermoFischer Scientific, Dreieich, Germany) was used as the protein ladder.

Phylogenetic analysis

Selected NifH, VnfH and AnfH sequences (accession numbers can be found in Table S1) were aligned using MUSCLE [88] (default parameters) in MEGA11 [89,90]. Ambiguous positions were removed for each possible pairing (pairwise deletion option). The final alignment contained a total of 332 NifH positions. The phylogenetic tree was constructed using the Neighbour-Joining method [91] with the Jones–Taylor–Thornton (JTT) matrix model for multiple substitutions [92]. The analysis was conducted in MEGA11 with ChlLNB from *Chlorobium limicola* as an outgroup. The tree was visualised and annotated with ITOL v5 [93].

Acknowledgements

We thank the Max Planck Society and Max Planck Institute for Marine Microbiology for their continuous support. We also thank Christina Probian and Ramona Appel for their technical assistance in the Microbial Metabolism laboratory, Olivier Lemaire for his validation of phylogenetic analyses, and Daniel Ratcliff for his help with the protein purification from *A. vinelandii*. We thank Dennis Dean for sharing plasmid pDB1282 and James Swartz for sharing the *E. coli* BL21 (DE3) Δ*iscR strain*. We thank the Swiss Light Source and SOLEIL Synchrotrons, especially the beamline staff for their advice during data collection. This study was funded by the Max Planck Society. The Oryx Nano robot used for the initial crystallisation screen was obtained through a grant from the Deutsche Forschungsgemeinschaft Schwerpunktprogram 1927 'Iron-sulfur for Life' (WA 4053/1-1). CC and RDM acknowledge funding from the NCCR Catalysis (grant number 180544), a National Centre of Competence in Research funded by the Swiss National Science Foundation. Open Access funding enabled and organized by Projekt DEAL.

Conflict of interest

The authors declare no conflict of interest.

Author contributions

NM and TW designed the research. WG cloned and prepared the plasmid for *Mm*NifH production. CC and NM purified *Av*NifDK and *Av*NifH. FM optimised the protocol for the purification of recombinant *Mi*NifH. PB cultivated *M. infernus* cells and purified native *Mi*NifH. NM cultivated *M. thermolithotrophicus* cells and purified native *Mt*NifH. NM produced recombinant *Mm*/*Mt*/*Mi*NifH. NM performed the phylogenetic analysis, activity assays, and hrCN PAGE. TW performed thermal denaturation experiment and UV/visible spectrophotometry. NM and TW crystallised nucleotide-free *Mt*NifH, NM crystallised *Mm*NifH and *Mt*NifH in the presence of MgADP, and PB crystallised *Mi*NifH in the presence of MgADP. X-ray data collection was performed by NM and TW Data processing, model building, structure refinement, validation and deposition were performed by NM and TW. Structures were analysed by NM and TW. RDM and TW acquired funding to realise the project. The paper was written by NM and TW with contributions and final approval of all co-authors.

Peer review

The peer review history for this article is available at https://www.webofscience.com/api/gateway/wos/peer-review/10.1111/febs.17148.

Data availability statement

The structural data that support these findings (see Table 1) are openly available in the wwPDB at: https://doi.org/10.2210/pdb8q5t/pdb, *Mt*NifH as isolated form 1; https://doi.org/10.2210/pdb8q50/pdb,

*Mt*NifH as isolated form 2; https://doi.org/10.2210/pdb8q5x/pdb, *Mm*NifH-MgADP, https://doi.org/10.2210/pdb8q5v/pdb, *Mt*NifH-MgADP and https://doi.org/10.2210/pdb8q5w/pdb, *Mi*NifH-MgADP. Access to the data that support the findings of this study can be provided by the corresponding author upon reasonable request.

References

1 Zhang X, Ward BB & Sigman DM (2020) Global nitrogen cycle: critical enzymes, organisms, and processes for nitrogen budgets and dynamics. *Chem Rev* **120**, 5308–5351.
2 Erisman JW, Sutton MA, Galloway J, Klimont Z & Winiwarter W (2008) How a century of ammonia synthesis changed the world. *Nat Geosci* **1**, 636–639.
3 Nayak-Luke R, Bañares-Alcántara R & Wilkinson I (2018) "Green" ammonia: impact of renewable energy intermittency on plant sizing and levelized cost of ammonia. *Ind Eng Chem Res* **57**, 14607–14616.
4 Smil V (2002) Nitrogen and food production: proteins for human diets. *Ambio* **31**, 126–131.
5 Philibert C (2017) Renewable Energy for Industry. Vol. **65**, International Energy Agency, Paris.
6 Ritter SK (2008) The Haber–Bosch reaction: an early chemical impact on sustainability. *Chem Eng News* **86**, 11.
7 Mus F, Alleman AB, Pence N, Seefeldt LC & Peters JW (2018) Exploring the alternatives of biological nitrogen fixation. *Metallomics* **10**, 523–538.
8 Atalah J, Cáceres-Moreno P, Espina G & Blamey JM (2019) Thermophiles and the applications of their enzymes as new biocatalysts. *Bioresour Technol* **280**, 478–488.
9 Tanabe Y & Nishibayashi Y (2021) Comprehensive insights into synthetic nitrogen fixation assisted by molecular catalysts under ambient or mild conditions. *Chem Soc Rev* **50**, 5201–5242.
10 Kirn J & Rees D (1992) Crystallographic structure and functional implications of the nitrogenase molybdenum–iron protein from *Azotobacter vinelandii*. *Nature* **360**, 553–560.
11 Kim J & Rees D (1992) Structural models for the metal centers in the nitrogenase molybdenum-iron protein. *Science* **257**, 1677–1682.
12 Einsle O & Rees DC (2020) Structural enzymology of nitrogenase enzymes. *Chem Rev* **120**, 4969–5004.
13 Eady RR (1996) Structure-function relationships of alternative nitrogenases. *Chem Rev* **96**, 3013–3030.
14 Boyd ES, Anbar AD, Miller S, Hamilton TL, Lavin M & Peters JW (2011) A late methanogen origin for molybdenum-dependent nitrogenase. *Geobiology* **9**, 221–232.
15 Garcia AK, McShea H, Kolaczkowski B & Kaçar B (2020) Reconstructing the evolutionary history of nitrogenases: evidence for ancestral molybdenum-cofactor utilization. *Geobiology* **18**, 394–411.
16 Jasniewski AJ, Lee CC, Ribbe MW, Ribbe MW & Hu Y (2020) Reactivity, mechanism, and assembly of the alternative nitrogenases. *Chem Rev* **120**, 5107–5157.
17 Koonin EV (1993) A superfamily of ATPases with diverse functions containing either classical or deviant ATP-binding motif. *J Mol Biol* **229**, 1165–1174.
18 Leipe DD, Wolf YI, Koonin EV & Aravind L (2002) Classification and evolution of P-loop GTPases and related ATPases. *J Mol Biol* **317**, 41–72.
19 Georgiadis M, Komiya H, Chakrabarti P, Woo D, Kornuc J & Rees D (1992) Crystallographic structure of the nitrogenase iron protein from *Azotobacter vinelandii*. *Science* **257**, 1653–1659.
20 Jasniewski AJ, Sickerman NS, Hu Y & Ribbe MW (2018) The Fe protein: an unsung hero of nitrogenase. *Inorganics* **6**, 25.
21 Burén S, Jiménez-Vicente E, Echavarri-Erasun C & Rubio LM (2020) Biosynthesis of nitrogenase cofactors. *Chem Rev* **120**, 4921–4968.
22 Howard JB & Rees DC (1994) Nitrogenase: a nucleotide-dependent molecular switch. *Annu Rev Biochem* **63**, 235–264.
23 Danyal K, Dean DR, Hoffman BM & Seefeldt LC (2011) Electron transfer within nitrogenase: evidence for a deficit-spending mechanism. *Biochemistry* **50**, 9255–9263.
24 Lanzilotta WN & Seefeldt LC (1997) Changes in the midpoint potentials of the nitrogenase metal centers as a result of iron protein-molybdenum-iron protein complex formation. *Biochemistry* **36**, 12976–12983.
25 Yang Z-Y, Ledbetter R, Shaw S, Pence N, Tokmina-Lukaszewska M, Eilers B, Guo Q, Pokhrel N, Cash VL & Dean DR (2016) Evidence that the P_i release event is the rate-limiting step in the nitrogenase catalytic cycle. *Biochemistry* **55**, 3625–3635.
26 Mortenson LE (1964) Ferredoxin and ATP, requirements for nitrogen fixation in cell-free extracts of *Clostridium pasteurianum*. *Proc Natl Acad Sci U S A* **52**, 272–279.
27 Martin A, Burgess B, Iismaa S, Smartt C, Jacobson M & Dean D (1989) Construction and characterization of an *Azotobacter vinelandii* strain with mutations in the genes encoding flavodoxin and ferredoxin I. *J Bacteriol* **171**, 3162–3167.
28 Burgess BK & Lowe DJ (1996) Mechanism of molybdenum nitrogenase. *Chem Rev* **96**, 2983–3012.
29 Schneider K & Müller A (2004) Iron-only nitrogenase: exceptional catalytic, structural and spectroscopic features. In Catalysts for Nitrogen Fixation: Nitrogenases, Relevant Chemical Models and

Commercial Processes (Smith BE, Richards RL & Newton WE, eds), pp. 281–307. Springer, Netherlands.
30 Harris DF, Lukoyanov DA, Kallas H, Trncik C, Yang Z-Y, Compton P, Kelleher N, Einsle O, Dean DR, Hoffman BM *et al.* (2019) Mo-, V-, and Fe-nitrogenases use a universal eight-electron reductive-elimination mechanism to achieve N_2 reduction. *Biochemistry* **58**, 3293–3301.
31 Badalyan A, Yang Z-Y & Seefeldt LC (2019) A voltammetric study of nitrogenase catalysis using electron transfer mediators. *ACS Catal* **9**, 1366–1372.
32 Seefeldt LC, Yang ZY, Lukoyanov DA, Harris DF, Dean DR, Raugei S & Hoffman BM (2020) Reduction of substrates by nitrogenases. *Chem Rev* **120**, 5082–5106.
33 Seefeldt LC, Yang Z-Y, Duval S & Dean DR (2013) Nitrogenase reduction of carbon-containing compounds. *Biochim Biophys Acta* **1827**, 1102–1111.
34 Hu Y & Ribbe MW (2015) Nitrogenase and homologs. *J Biol Inorg Chem* **20**, 435–445.
35 Rebelein JG, Stiebritz MT, Lee CC & Hu Y (2017) Activation and reduction of carbon dioxide by nitrogenase iron proteins. *Nat Chem Biol* **13**, 147–149.
36 Stiebritz MT, Hiller CJ, Sickerman NS, Lee CC, Tanifuji K, Ohki Y & Hu Y (2018) Ambient conversion of CO_2 to hydrocarbons by biogenic and synthetic $[Fe_4S_4]$ clusters. *Nat Catal* **1**, 444–451.
37 Rohde M, Trncik C, Sippel D, Gerhardt S & Einsle O (2018) Crystal structure of VnfH, the iron protein component of vanadium nitrogenase. *J Biol Inorg Chem* **23**, 1049–1056.
38 Trncik C, Müller T, Franke P & Einsle O (2022) Structural analysis of the reductase component AnfH of iron-only nitrogenase from *Azotobacter vinelandii*. *J Inorg Biochem* **227**, 111690.
39 Schlessman JL, Woo D, Joshua-Tor L, Howard JB & Rees DC (1998) Conformational variability in structures of the nitrogenase iron proteins from *Azotobacter vinelandii* and *Clostridium pasteurianum*. *J Mol Biol* **280**, 669–685.
40 Rettberg LA, Kang W, Stiebritz MT, Hiller CJ, Lee CC, Liedtke J, Ribbe MW & Hu Y (2019) Structural analysis of a nitrogenase iron protein from *Methanosarcina acetivorans*: implications for CO_2 capture by a surface-exposed $[Fe_4S_4]$ cluster. *MBio* **10**, e01497-19.
41 Boyd ES, Hamilton TL & Peters JW (2011) An alternative path for the evolution of biological nitrogen fixation. *Front Microbiol* **2**, 205.
42 Maslać N, Sidhu C, Teeling H & Wagner T (2022) Comparative transcriptomics sheds light on remodeling of gene expression during diazotrophy in the thermophilic methanogen *Methanothermococcus thermolithotrophicus*. *MBio* **13**, e02443-22.
43 Liu Y & Whitman WB (2008) Metabolic, phylogenetic, and ecological diversity of the methanogenic archaea. *Ann N Y Acad Sci* **1125**, 171–189.
44 Miller JF, Shah NN, Nelson CM, Ludlow JM & Clark DS (1988) Pressure and temperature effects on growth and methane production of the extreme thermophile *Methanococcus jannaschii*. *Appl Environ Microbiol* **54**, 3039–3042.
45 Kendall MM, Liu Y, Sieprawska-Lupa M, Stetter KO, Whitman WB & Boone DR (2006) *Methanococcus aeolicus* sp. nov., a mesophilic, methanogenic archaeon from shallow and deep marine sediments. *Int J Syst Evol Microbiol* **56**, 1525–1529.
46 Lecocq M, Groussin M, Gouy M & Brochier-Armanet C (2020) The molecular determinants of Thermoadaptation: *Methanococcales* as a case study. *Mol Biol Evol* **38**, 1761–1776.
47 Mehta MP, Butterfield DA & Baross JA (2003) Phylogenetic diversity of nitrogenase (*nifH*) genes in Deep-Sea and hydrothermal vent environments of the Juan de Fuca ridge. *Appl Environ Microbiol* **69**, 960–970.
48 Man-Aharonovich D, Kress N, Zeev EB, Berman-Frank I & Béjà O (2007) Molecular ecology of *nifH* genes and transcripts in the eastern Mediterranean Sea. *Environ Microbiol* **9**, 2354–2363.
49 Dang H, Luan X, Zhao J & Li J (2009) Diverse and novel *nifH* and *nifH*-like gene sequences in the Deep-Sea methane seep sediments of the Okhotsk Sea. *Appl Environ Microbiol* **75**, 2238–2245.
50 Bae HS, Morrison E, Chanton JP & Ogram A (2018) Methanogens are major contributors to nitrogen fixation in soils of the Florida Everglades. *Appl Environ Microbiol* **84**, 1–16.
51 Belay N, Sparling R & Daniels L (1984) Dinitrogen fixation by a thermophilic methanogenic bacterium. *Nature* **312**, 286–288.
52 Mehta MP & Baross JA (2006) Nitrogen fixation at 92 °C by a hydrothermal vent archaeon. *Science* **314**, 1783–1786.
53 Enzmann F, Mayer F, Rother M & Holtmann D (2018) Methanogens: biochemical background and biotechnological applications. *AMB Express* **8**, 1.
54 Jones WJ, Paynter MJB & Gupta R (1983) Characterization of *Methanococcus maripaludis* sp. nov., a new methanogen isolated from salt marsh sediment. *Arch Microbiol* **135**, 91–97.
55 Huber H, Thomm M, König H, Thies G & Stetter KO (1982) *Methanococcus thermolithotrophicus*, a novel thermophilic lithotrophic methanogen. *Arch Microbiol* **132**, 47–50.
56 Jeanthon C, L'Haridon S, Reysenbach AL, Vernet M, Messner P, Sleytr UB & Prieur D (1998) *Methanococcus infernu*s sp. nov., a novel hyperthermophilic lithotrophic methanogen isolated from a deep-sea hydrothermal vent. *Int J Syst Evol Microbiol* **48**, 913–919.
57 Robert X & Gouet P (2014) Deciphering key features in protein structures with the new ENDscript server. *Nucleic Acids Res* **42**, W320–W324.

58 Tezcan FA, Kaiser JT, Mustafi D, Walton MY, Howard JB & Rees DC (2005) Nitrogenase complexes: multiple docking sites for a nucleotide switch protein. *Science* **309**, 1377–1380.
59 Rutledge HL & Tezcan FA (2020) Electron transfer in nitrogenase. *Chem Rev* **120**, 5158–5193.
60 Krissinel E & Henrick K (2007) Inference of macromolecular assemblies from crystalline state. *J Mol Biol* **372**, 774–797.
61 Cadoux C, Maslać N, Di Luzio L, Ratcliff D, Gu W, Wagner T & Milton RD (2023) The mononuclear metal-binding site of Mo-nitrogenase is not required for activity. *JACS Au* **3**, 2993–2999.
62 Bröcker MJ, Virus S, Ganskow S, Heathcote P, Heinz DW, Schubert W-D, Jahn D & Moser J (2008) ATP-driven reduction by dark-operative protochlorophyllide oxidoreductase from *Chlorobium tepidum* mechanistically resembles nitrogenase catalysis. *J Biol Chem* **283**, 10559–10567.
63 Hiller CJ, Stiebritz MT, Lee CC, Liedtke J & Hu Y (2017) Tuning electron flux through nitrogenase with methanogen iron protein homologues. *Chemistry* **23**, 16152–16156.
64 Jasper J, Ramos JV, Trncik C, Jahn D, Einsle O, Layer G & Moser J (2020) Chimeric interaction of nitrogenase-like reductases with the MoFe protein of nitrogenase. *Chembiochem* **21**, 1733–1741.
65 Cadoux C, Ratcliff D, Maslać N, Gu W, Tsakoumagkos I, Hoogendoorn S, Wagner T & Milton RD (2023) Nitrogen fixation and hydrogen evolution by sterically encumbered Mo-nitrogenase. *JACS Au* **3**, 1521–1533.
66 Schindelin H, Kisker C, Schlessman JL, Howard JB & Rees DC (1997) Structure of ADP·AlF_4^--stabilized nitrogenase complex and its implications for signal transduction. *Nature* **387**, 370–376.
67 Renner KA & Howard JB (1996) Aluminum fluoride inhibition of nitrogenase: stabilization of a nucleotide·Fe-protein·MoFe-protein complex. *Biochemistry* **35**, 5353–5358.
68 Udvardi M, Brodie EL, Riley W, Kaeppler S & Lynch J (2015) Impacts of agricultural nitrogen on the environment and strategies to reduce these impacts. *Procedia Environ Sci* **29**, 303.
69 Olabi AG, Abdelkareem MA, Al-Murisi M, Shehata N, Alami AH, Radwan A, Wilberforce T, Chae K-J & Sayed ET (2023) Recent progress in green ammonia: production, applications, assessment; barriers, and its role in achieving the sustainable development goals. *Energ Conver Manage* **277**, 116594.
70 Ornes S (2021) Green ammonia could produce climate-friendly ways to store energy and fertilize farms. *Proc Natl Acad Sci U S A* **118**, e2119584118.
71 Garcia AK, Harris DF, Rivier AJ, Carruthers BM, Pinochet-Barros A, Seefeldt LC & Kaçar B (2023) Nitrogenase resurrection and the evolution of a singular enzymatic mechanism. *Elife* **12**, e85003.
72 Ray S, Kuppam C, Pandit S & Kumar P (2023) Biogas upgrading by hydrogenotrophic methanogens: an overview. *Waste Biomass Valori* **14**, 537–552.
73 Zabranska J & Pokorna D (2018) Bioconversion of carbon dioxide to methane using hydrogen and hydrogenotrophic methanogens. *Biotechnol Adv* **36**, 707–720.
74 Dodsworth JA & Leigh JA (2006) Regulation of nitrogenase by 2-oxoglutarate-reversible, direct binding of a PII-like nitrogen sensor protein to dinitrogenase. *Proc Natl Acad Sci U S A* **103**, 9779–9784.
75 Leigh JA & Dodsworth JA (2007) Nitrogen regulation in bacteria and archaea. *Annu Rev Microbiol* **61**, 349–377.
76 Costa KC, Wong PM, Wang T, Lie TJ, Dodsworth JA, Swanson I, Burn JA, Hackett M & Leigh JA (2010) Protein complexing in a methanogen suggests electron bifurcation and electron delivery from formate to heterodisulfide reductase. *Proc Natl Acad Sci U S A* **107**, 11050–11055.
77 Vonrhein C, Flensburg C, Keller P, Sharff A, Smart O, Paciorek W, Womack T & Bricogne G (2011) Data processing and analysis with the *autoPROC* toolbox. *Acta Crystallogr D* **67**, 293–302.
78 Tickle I, Flensburg C, Keller P, Paciorek W, Sharff A, Vonrhein C & Bricogne G (2018) Staraniso. Global Phasing Ltd, Cambridge, UK.
79 McCoy AJ, Grosse-Kunstleve RW, Adams PD, Winn MD, Storoni LC & Read RJ (2007) Phaser crystallographic software. *J Appl Cryst* **40**, 658–674.
80 Liebschner D, Afonine PV, Baker ML, Bunkóczi G, Chen VB, Croll TI, Hintze B, Hung LW, Jain S, McCoy AJ *et al.* (2019) Macromolecular structure determination using X-rays, neutrons and electrons: recent developments in phenix. *Acta Crystallogr D* **75**, 861–877.
81 Emsley P, Lohkamp B, Scott WG & Cowtan K (2010) Features and development of Coot. *Acta Crystallogr D* **66**, 486–501.
82 Williams CJ, Headd JJ, Moriarty NW, Prisant MG, Videau LL, Deis LN, Verma V, Keedy DA, Hintze BJ, Chen VB *et al.* (2018) MolProbity: more and better reference data for improved all-atom structure validation. *Protein Sci* **27**, 293–315.
83 Milton RD, Cai R, Abdellaoui S, Leech D, De Lacey AL, Pita M & Minteer SD (2017) Bioelectrochemical Haber–Bosch process: an ammonia-producing H_2/N_2 fuel cell. *Angew Chem Int Ed* **56**, 2680–2683.
84 Corbin JL (1984) Liquid chromatographic-fluorescence determination of ammonia from nitrogenase reactions: a 2-min assay. *Appl Environ Microbiol* **47**, 1027–1030.
85 Brown KA, Harris DF, Wilker MB, Rasmussen A, Khadka N, Hamby H, Keable S, Dukovic G, Peters JW & Seefeldt LC (2016) Light-driven dinitrogen

reduction catalyzed by a CdS: nitrogenase MoFe protein biohybrid. *Science* **352**, 448–450.
86 Milton RD, Abdellaoui S, Khadka N, Dean DR, Leech D, Seefeldt LC & Minteer SD (2016) Nitrogenase bioelectrocatalysis: heterogeneous ammonia and hydrogen production by MoFe protein. *Energ Environ Sci* **9**, 2550–2554.
87 Lemaire ON, Infossi P, Ali Chaouche A, Espinosa L, Leimkühler S, Giudici-Orticoni M-T, Méjean V & Iobbi-Nivol C (2018) Small membranous proteins of the TorE/NapE family, crutches for cognate respiratory systems in proteobacteria. *Sci Rep* **8**, 13576.
88 Edgar RC (2004) MUSCLE: a multiple sequence alignment method with reduced time and space complexity. *BMC Bioinformatics* **5**, 113.
89 Kumar S, Stecher G, Li M, Knyaz C & Tamura K (2018) MEGA X: molecular evolutionary genetics analysis across computing platforms. *Mol Biol Evol* **35**, 1547–1549.
90 Tamura K, Stecher G & Kumar S (2021) MEGA11: molecular evolutionary genetics analysis version 11. *Mol Biol Evol* **38**, 3022–3027.
91 Saitou N & Nei M (1987) The neighbor-joining method: a new method for reconstructing phylogenetic trees. *Mol Biol Evol* **4**, 406–425.
92 Jones DT, Taylor WR & Thornton JM (1992) The rapid generation of mutation data matrices from protein sequences. *Comput Appl Biosci* **8**, 275–282.
93 Letunic I & Bork P (2021) Interactive tree of life (iTOL) v5: an online tool for phylogenetic tree display and annotation. *Nucleic Acids Res* **49**, W293–W296.
94 Rees DC, Akif Tezcan F, Haynes CA, Walton MY, Andrade S, Einsle O & Howard JB (2005) Structural basis of biological nitrogen fixation. *Philos Trans Roy Soc A Math Phys Eng Sci* **363**, 971–984.
95 Seefeldt LC, Peters JW, Beratan DN, Bothner B, Minteer SD, Raugei S & Hoffman BM (2018) Control of electron transfer in nitrogenase. *Curr Opin Chem Biol* **47**, 54–59.

Supporting information

Additional supporting information may be found online in the Supporting Information section at the end of the article.

Fig. S1. SDS/PAGE of purified proteins.

Fig. S2. Structural comparison between *Mt*NifH dimers in the apo state.

Fig. S3. Method description to estimate melting points of studied proteins under an anaerobic atmosphere.

Table S1. Accession numbers for sequences used in phylogenetic reconstruction.

Table S2. Conservation of NifH residues interacting with NifDK.

Table S3. Vectors, and strains used in this study.